

Apertureless near-field optical microscopy

D V Kazantsev, E V Kuznetsov, S V Timofeev, A V Shelaev, E A Kazantseva

DOI: <https://doi.org/10.3367/UFNe.2016.05.037817>

Contents

1. Introduction	259
2. Operational principle of an apertureless scanning near-field optical microscope (ASNOM)	260
2.1 Relation between the fields of an irradiating (emitted) wave and the local field under the tip; 2.2 Elastic scattering of a driving light wave; 2.3 Optical homodyning; 2.4 Spectroscopy of elastic light scattering in an ASNOM	
3. Material contrast in ASNOM images	264
3.1 Approach curve dependence on the dielectric constant; 3.2 Mapping of semiconducting structures with an ASNOM of elastic scattering (sSNOM); 3.3 sSNOM imaging of biological objects; 3.4 ASNOM imaging of polymers; 3.5 Undersurface imaging of ‘buried’ objects; 3.6 Visualization of surface polariton waves	
4. Ultrashort light pulses	271
5. Spectroscopy with an ASNOM	271
5.1 Tip-enhanced Raman scattering (TERS); 5.2 Photoluminescence	
6. Conclusions. Summary	273
6.1 What should an ‘ideal’ ASNOM look like?	
References	274

Abstract. We discuss the operating principles of the apertureless scanning near-field optical microscope (ASNOM), in which the probe acts as a rod antenna and its electromagnetic radiation plays the role of the registered signal. The phase and amplitude of the emitted wave vary depending on the ‘grounding conditions’ of the antenna tip at the sample point under study. Weak radiation from a tiny (2–15 μm long) tip is detected using optical homo- and heterodyning and the nonlinear dependence of the tip polarizability on the tip–surface distance. The lateral resolution of ASNOMs is determined by the tip curvature radius (1–20 nm), regardless of the wavelength (500 nm–100 μm). ASNOMs are shown to be capable of providing a surface optical map with nanometer resolution and carrying out spectral- and time-resolved measurements at a selected point on the surface.

Keywords: scanning near-field microscopy, Raman scattering, nanostructures, ASNOM

D V Kazantsev National Research Center “Kurchatov Institute,”
Alikhanov Institute of Theoretical and Experimental Physics,
ul. B. Cheremushkinskaya 25, 117218 Moscow, Russian Federation
E-mail: kaza@itep.ru
E V Kuznetsov, S V Timofeev, A V Shelaev NT-MDT Spectrum
Instruments: “NT-MDT,”
proezd 4922, 4/3, 124460 Zelenograd, Moscow, Russian Federation
E-mail: kuznetsov@ntmdt.ru, sergey_t@ntmdt.ru, shelaev@ntmdt.ru
E A Kazantseva Moscow Technological University,
prosp. Vernadskogo 78, 119454 Moscow, Russian Federation
E-mail kanele19@gmail.com

Received 15 April 2016, revised 24 May 2016

Uspekhi Fizicheskikh Nauk **187** (3) 277–295 (2017)

DOI: <https://doi.org/10.3367/UFNr.2016.05.037817>

Translated by D V Kazantsev; edited by A M Semikhatov

1. Introduction

In the last 10–20 years, scanning near-field optical microscopy (SNOM, NFOM) with an option of optical spectroscopy has demonstrated significant success as a method to investigate optical properties of surfaces. Like all other similar scanning probe microscopy (SPM) methods, near-field optical microscopy [1] was first proposed in 1984, soon after scanning tunneling microscopy [2] (STM). STM first demonstrated its simple and reliable technical ability of positioning a sub-nm sharp probe relative to objects located on a sample surface. The invention of an STM was therefore a triggering event for the development of all other SPM techniques.

Disadvantages of an aperture-defined SNOM. In the first SNOMs [3–5], the tapered tip of an optical fiber was used as a probe. To define a light-sensitive area on the tip apex, a small (50–100 nm) hole was made in a metal mask covering the tip [6]. The size of that pinhole determined the optical lateral resolution of an instrument. Unfortunately, the light transmission of such a pinhole in a metal layer [7] drops much faster than the physical area of the hole itself, $(1/4)\pi a^2$. This can be seen from the expression for the effective area of light transmission calculated for a hole of diameter a formed in an opaque metal plane:

$$\sigma = a^2 \frac{64}{27\pi} \left(\frac{2\pi a}{\lambda} \right)^4 \left(1 - \frac{3}{8} \sin \theta \right). \quad (1)$$

Here, σ is the effective area of light transmission and θ is the incidence angle of the initial plane wave. As a result, an improvement in the lateral resolution very quickly leads to the disappearance of the signal being collected.

The light transmission of an optical probe formed by mechanical tapering of a fiber is also reduced by the small diameter

of its sharpened part. Any simply connected (1-connected) waveguide has a low cut-off frequency, and the frequency of light used in SNOM experiments is typically lower than the cut-off frequency of the narrow part of the tapered fiber. As a consequence, the light decays exponentially along the fiber on its way in the tapered part of the probe. This general law was especially considered for metal-coated tapered fibers [8]. It was found experimentally in [9] that only about 10^{-5} of the light radiation injected into a fiber is emitted out of the aperture hole.

One more effect that reduces the optical resolution in a conventional (aperture-defined) SNOM is the electromagnetic blur of the metal aperture edge caused by plasmonic phenomena in the metal. The skin-layer depth in a metal is about 5–6 nm in the visible-light frequency band. A ring-like image of a luminescent-active cluster known to be a point-like source [10] causes some doubts. We can assume that the light oscillations from a source are not simply transmitted into the fiber probe through the aperture (in that case, the image from a few-nm source produced by a relatively large aperture would have the shape of the aperture). Instead, the light fields of an object under study excite the plasmonic waves on (in) the metal at the nearest point of the mask edge (the points are different due to raster scanning of the probe with respect to the sample). These plasmon waves somehow propagate along the tip, and some fraction of the light finally ‘leaks’ into the fiber core to be collected as a luminescence signal.

Thus, the aperture-defined modification of SNOM suffers from two fundamental limitations. Radiative modes of an electromagnetic field are squeezed too tightly inside the probe fiber, and nonradiative (near-field) modes around the probe are confined too little.

2. Operational principle of an apertureless scanning near-field optical microscope (ASNOM)

A breakthrough in the evolution of the technique occurred at the turn of the century (2000) due to the change from conventional (aperture-defined) SNOM to its apertureless modification [11–13]. The basic principle of an apertureless SNOM (Fig. 1) is [14] the implementation of a tapered metal wire to couple the electromagnetic processes in the object being studied to the fields of the electromagnetic waves in the optical band. The wire mentioned above is similar to a rod antenna in classical radio.

First, the electric oscillation in such a wire—both dipole oscillations of the charge density and more complicated plasmon excitations—easily emit light waves into the ambient space and, in turn, can easily be excited by light waves coming from outside. Second, such a probe placed close enough to the object to be investigated (e.g., a nanocrystal, a virus, or a single molecule) comes into electromagnetic interaction with the object, mainly with the electric near-field modes. These electric fields are typically not emitted into the ambient space (their coupling to propagating electromagnetic waves is weak) and therefore cannot be optically excited or detected from outside. But near fields provide a rather strong electromagnetic coupling between the object being studied and dipole oscillations inside the probe. The gap between the probe and the sample acts in this case as a capacitor in a conventional radio.

The lateral resolution of an instrument (0.8 nm [15], 1 nm [12], 10 nm [16], or 50 nm [17]) is therefore determined by the dimensions of such a ‘capacitor’ corresponding to the tip

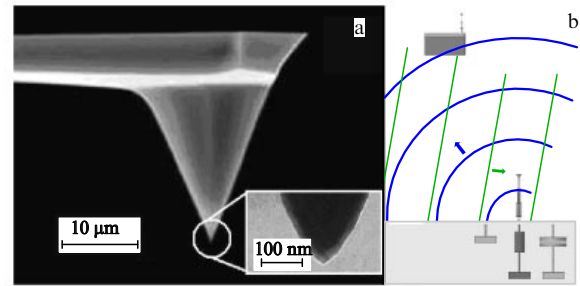


Figure 1. (a) SEM image of a commercially available tip (Micromash CSC-37-Pt) on the AFM cantilever and an enlarged image of the tip apex. The tip is coated with platinum to serve the needs of the ASNOM method. Images are taken from the Micromash website. (b) ASNOM in terms of a radio: the metallized tip is equivalent to a rod antenna, the dipole oscillations in it driven by an external field depend on the grounding conditions of the antenna end. The amplitude and phase of the divergent wave re-emitted by such an antenna can be reliably detected.

radius, regardless of the wavelength being used. In the electrostatic approximation, it can also be claimed [18] that the field amplitude E_{loc} in the gap between the tip and the sample can be expressed in terms of the gap width d and the tip potential oscillation amplitude U_{tip} as U_{tip}/d . In such a model, the amplitude of the local field can become arbitrarily high (as $d \rightarrow 0$).

Because of the reasons listed above, ASNOM has become widely accepted (see reviews [19, 20]) as an optical method of surface investigations with nanometer resolution. Radiative electromagnetic modes have enough space around the tip; nonradiative (near-field) modes are confined to just the tip-sample gap. Such antenna-like probes are widely offered by a variety of vendors as part of cheap Si cantilevers, similar to those used in an AFM [21] mounted on a carrier chip to make reload easy. To fit the ASNOM method requirements, the tips are typically coated with a metal layer, a good choice being Pt [22], which has rather good conductivity in the optical band and is also mechanically hard enough to resist tip wearing caused by the tip-sample contact. The radius of the tip in this case is 10–40 nm.

2.1 Relation between the fields of an irradiating (emitted) wave and the local field under the tip

For theoretical considerations, an obvious point of interest is the degree to which the presence of an ASNOM tip increases the efficiency of interaction between an external electromagnetic wave and a nano-object located in the tip-substrate gap. The simplest model of a probe [12] (a point-like dipole located above a surface with a dielectric function ϵ_s) is not able to predict any field enhancement under the tip. A probing tip near the surface was considered in various papers as a pyramid [23], hyperboloid [24], or spheroid [25–27]. Simulations in [28] using spherical and ellipsoidal shapes of the tip also include a small gold sphere located between the tip and the surface to model the nano-object being investigated. Numerical simulations [29] (using commercially available HFSSTM software [30]) in which the tip was represented as a pyramid with a blunted tip apex (the most realistic model) were able to also consider the excitation and contribution of the plasmonic waves running along the tip from its apex and thus to extend the consideration beyond the electrostatic approximation used in analytic calculations.

In these models, typical ASNOM dependences were calculated, namely, the approach curve [28] (signal depen-

dence on the tip–sample distance) and spectral and angular diagrams [29] of the signal scattered by the tip in the presence of the surface. It was shown that the angle-of-elevation diagram (which generally depends on the tip and sample media) typically has one or two directional lobes. In all cases, the optimal angle to couple external radiation to an ASNOM tip is 60° – 70° to the normal to the sample surface. The influence of the irradiation angle and polarization is also mentioned in [23]. The simple dipole antenna behavior has been described for the radio frequency band [31–33]; however, calculations of the optical fields applied to a particular case of an ASNOM are certainly useful.

Significant field enhancement (4–5 orders of magnitude) in the gap between the tip and the sample compared to the field of an irradiating (emitted) wave is mentioned in many papers [26, 34–36] and proved experimentally [24]. Theoretical considerations of the fields excited around an ASNOM tip by external radiation in the presence of a sample surface, as well as the fields emitted by an ASNOM tip into the ambient space, vary in their details and methods. Nevertheless, they are similar in the following: (1) the electric field amplitude near the tip apex is several orders higher than the amplitude of the driving wave; (2) tip–sample interaction is significantly enhanced at distances of about the tip curvature radius; (3) effects arise mainly for a polarization of an external wave such that the E_{loc} vector is normal to the surface (directed along the tip shaft). For another light polarization, the field enhancement is weak or completely absent.

2.2 Elastic scattering of a driving light wave

Presently, the most widely used mode of ASNOMs is ‘elastic light scattering’, which is often abbreviated as sSNOM (scattering SNOM). In the commonly accepted model [37, 38], which works rather well despite its simplicity, the tip is considered a ball with a dielectric permeability ϵ_t , and its polarizability in a homogeneous driving field is calculated in the long-wave approximation [39]. Emission of the scattered electromagnetic field by the tip into space is caused by dipole oscillations in such a ball. Disregarding propagation delays, the role of the sample surface can be well described by the electrostatic image of a ball representing the tip in that model, with the dielectric function of the surface ϵ_s and the dielectric function ϵ_i of the surrounding medium taken into account. In such a case, the effective dipole polarizability of the tip with its electrostatic image on the surface can be expressed as

$$\alpha_{\text{eff}} = \frac{\alpha(1 + \beta)}{1 - \alpha\beta/(16\pi(a + z)^3)}, \quad (2)$$

where

$$\alpha = 4\pi a^3 \frac{\epsilon_t - \epsilon_i}{\epsilon_t + 2\epsilon_i}, \quad \beta = \frac{\epsilon_s - 1}{\epsilon_s + 1}.$$

The radius of the sphere that represents the tip in the model is denoted here by a , the complex value of the sample dielectric permeability is denoted by ϵ_t , the tip dielectric function is written as ϵ_s (as a rule, corresponding to a platinum coating of ASNOM tips), and ϵ_i denotes the dielectric function of the medium in which the tip and sample are embedded (as a rule, air; the value $\epsilon_i = 1$ for the vacuum is typically used). Thus, at a large distance (indicated in expression (3) by the ∞ symbol), the scattered wave amplitude E_{scatt} is proportional to the amplitude E_{loc} of the electromagnetic field that excites the

oscillation in the tip, and also to the effective polarizability α_{eff} of the tip:

$$E_{\text{scatt}}(\infty) \sim E_{\text{loc}}\alpha_{\text{eff}} = E_{\text{loc}}(\mathbf{r}_{\text{tip}})\alpha_{\text{eff}}(\mathbf{r}_{\text{tip}}, \epsilon_s(\mathbf{r}_{\text{tip}})). \quad (3)$$

This can be rewritten for clarity as

$$E_{\text{scatt}}(\infty) \sim E_{\text{loc}}(\mathbf{r}_{\text{tip}XY})\alpha_{\text{eff}}(r_{\text{tip}Z}, \epsilon_s(\mathbf{r}_{\text{tip}XY})). \quad (4)$$

where the coordinate of the tip relative to the sample surface is \mathbf{r}_{tip} in general. To make reading more easy, we note that the local field E_{loc} that drives the dipole oscillations in the tip depends mostly on the tip coordinates in the sample plane (indicated by the subscript in $\mathbf{r}_{\text{tip}XY}$). Changes to the effective polarizability of the tip are mainly caused by the sample dielectric function at the tip location (denoted by $\epsilon_s(\mathbf{r}_{\text{tip}XY})$ in our expressions) as well as the tip–sample distance (denoted by $r_{\text{tip}Z}$).

Scattering of light by a tip in the presence of a surface (with the wavelength remaining constant in such a process) has been calculated in many papers [19, 25, 40–43]. Taking the frequency dependence of the sample dielectric function into account, the authors were able to calculate the scattering spectra of the probing tip. These simulations perfectly fit experimental results for metals (Au [44], Al, W [41]), non-resonant dielectrics (quartz, polystyrene, PMMA) [44, 45], Si_3N_4 , Si [41, 46], and resonant dielectrics (SiC [25, 42]). A good quantitative fit to the experimental data (maps of the ASNOM amplitude and phase) is demonstrated in analytic calculations [12, 39, 42] that take the contribution of the free carriers to the dielectric function of doped semiconductors into account [41, 47].

In the model of a ‘dipole over a dielectric surface,’ the following statements are important:

- (1) the amplitude of the light wave scattered by the tip into the external space under the influence of an incident coherent wave in the presence of a sample surface is, as a complex number, proportional to the local electromagnetic field amplitude;
- (2) the amplitude of the wave scattered by the tip depends on the tip–surface distance nonlinearly;
- (3) the amplitude of the scattered wave is determined by the local value of the surface dielectric function at the frequency of light near the tip (at the tip contact spot whose size is close to the tip radius).

These features allow ASNOMs to work in the ‘elastic light scattering’ mode (scattering at the frequency of the irradiating wave) for mapping the distribution of a local light field over the surface or (and) mapping a sample dielectric function.

It was mentioned in [40], however, that some parameters have to be adjusted for the theoretical simulations to fit the experimental data (first and foremost, the gap between the tip and the surface has to be adjusted). The inverse problem, i.e., reconstructing the dielectric permeability of the surface from the ASNOM signal, is fraught with difficulty and ambiguity.

2.3 Optical homodyning

The amplitude of a light wave scattered by the tip in the presence of a surface and then collected in a photodetector as a signal is, naturally, vanishingly low. An efficient technical trick to detect such a weak signal [48] is optical homodyning [12, 49, 50] or heterodyning [51, 52] (Fig. 2). The photodetector signal in that case is determined by the square of the light wave amplitude $I_{\text{det}} \sim E_{\text{det}}^2 = (E_{\text{ref}} + E_{\text{scatt}})^2$. In the

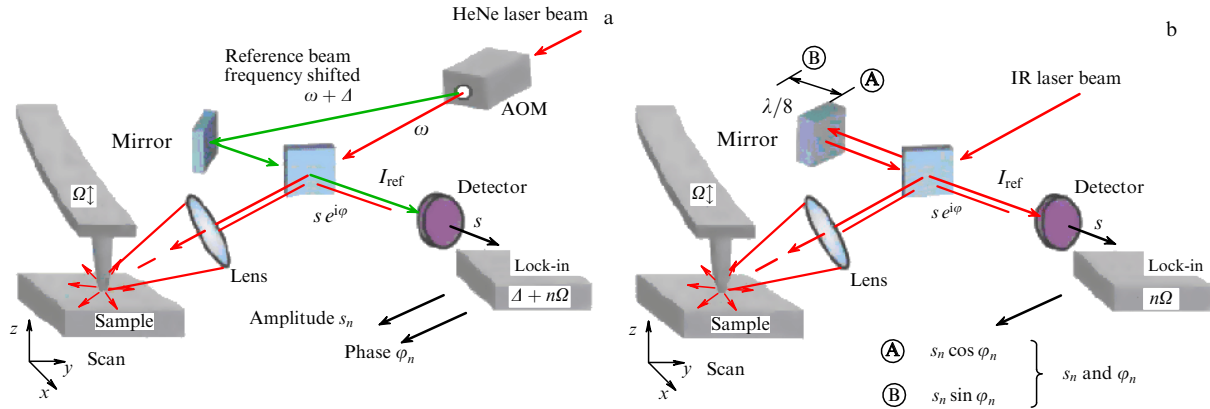


Figure 2. Optical (a) heterodyning and (b) homodyning of light scattered by an ASNO probe in the elastic scattering mode (sSNOM). (a) An HeNe laser beam is partially scattered by the acoustic–optical modulator AOM into a reference beam. The direction of this ray is determined by the combination of the wave vectors of light and sound in the AOM crystal, and the optical frequency is shifted by the sound frequency Δ . This beam is redirected by a mirror to the photodetector. The objective lens collects radiation scattered by the probe tip that is in optical contact with the sample and directs this light also to a photodetector. (b) In the optical homodyning (Michelson) scheme, the laser beam partially passes through a beamsplitter BS onto the sample and the tip. Another part of the laser beam is reflected into the reference arm, whose length is modulated in the measurement process by displacing the mirror. The higher harmonics of a frequency Ω of normal tip oscillations are recovered in the photocurrent by a lock-in detector at the frequency $\Delta + n\Omega$ in the heterodyne and $n\Omega$ in the homodyne setups [51].

expression

$$(E_{\text{ref}} + E_{\text{scatt}})^2 = E_{\text{ref}}^2 + 2E_{\text{ref}}E_{\text{scatt}} + E_{\text{scatt}}^2, \quad (5)$$

the term E_{ref} is constant, and therefore the leading contribution to changes in the detected signal is made by the term $2E_{\text{ref}}E_{\text{scatt}}$. The term E_{scatt}^2 would play a role in the absence of a reference wave that is coherent to the signal one. The term E_{scatt} in the expressions above denotes the amplitude of scattered light, and E_{ref} corresponds to a reference beam. Hence, the sensitivity of the detector can be improved by $E_{\text{ref}}/E_{\text{scatt}}$ times, i.e., several orders of magnitude, because the scattered wave is rather weak [53]. The expressions are written here in terms of real numbers for simplicity, but a rigorous consideration with complex numbers leads to the same conclusion.

As is clear from (2)–(4), the effective tip polarizability depends on the tip–surface distance in a highly nonlinear way, because near fields quickly decay with distance. This dependence was experimentally obtained in [54] by optical homodyning in a Michelson interferometer (Fig. 3). The

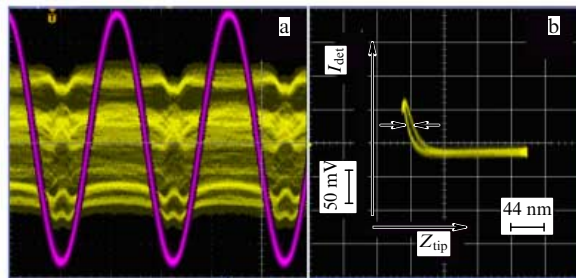


Figure 3. (a) Photocurrent signal [56] at the output of a Michelson interferometer at different lengths of the reference arm. The horizontal scale corresponds to the time, the vertical scale represents the position of the tip (sine curve) and photocurrent (pulses of various phases). The Pt-covered tip touches the SiC surface at the lower point of the sine curve. (b) Dependence of the detector signal at an output of the ASNO interferometer (proportional to the amplitude of the electric field in the scattered wave) on the tip height over a crystalline SiC surface, recorded in [54] as a Lissajous figure with the first two signals.

photodetector output (homodyned optical signal) and the tip displacement signal were used to plot a Lissajous figure. Unlike the previously published dependence of the second harmonic component of the tip oscillation frequency on the tip–surface distance [55], experiment [54] is a direct measurement, i.e., a direct dependence of the photocurrent on the tip position is maintained.

A detector located at the output of a Michelson interferometer [56] was connected to the vertical displacement of an oscilloscope beam, and the signal from the cantilever displacement was connected to a horizontal input. In the experiment, the amplitude of the tip vertical vibration was about 60 nm, and this signal caused a horizontal sweep. The ASNO tip in that experiment was in ‘working contact’ with the surface of crystalline SiC (known for its strong ASNO response in the wavelength band 10.41–12.70 μm caused by SiC lattice resonance). The tip, as well as the surrounding area of the SiC surface, was irradiated by a focused beam of a tunable $^{13}\text{C}^{16}\text{O}_2$ laser.

It can be seen that the detector output signal is first constant (the right part of the curve in Fig. 3b) and then changes within the left 30 nm of the plot. The polarity and height of this feature (see Fig. 3) depend on the reference beam phase in the interferometer in a sinusoidal way, as it must be for an interference response. We note that the Lissajous plot in Fig. 3b contains an area (the leftmost 5–7 nm on the plot) in which the detector signal apparently weakens. In reality, such a change is caused by a phase shift of the scattered signal near the surface, and this can be seen in similar Lissajous figures taken at other values of the reference phase. An important conclusion from Fig. 3 is that the amplitude and phase of variations in the radiation scattered by an ASNO tip depend on the tip–surface distance in a highly nonlinear manner, such that ‘touching the sample’ modulates the optical response just at distances of about 10–40 nm. The changes due to the near field in the optical response appear in the oscilloscope trace as bell-shaped peaks at the time of touching (bottom points of the tip displacement sine curve). It is also useful to mention that the polarity (phase) of these features depends on the reference beam phase (determined by the mirror position in a Michelson interferometer).

Nonlinearity in the optical signal dependence on the tip–surface gap allows recovering just those components in the optical signal that are exclusively caused by the near-field (short-range) optical interaction between the tip and the surface being investigated. Periodic modulation of the tip–sample distance is typically present in ASNO systems, e.g., resonant cantilever vibration used in TappingMode™ topography feedback [57]. This sinusoidal tip vibration modulates the complex amplitude of the light wave scattered by the tip. The nonlinearity of the near-field optical interaction between the tip and the sample at the separating distance is the only significant nonlinearity in the system. Therefore, recovering the higher harmonic components $I_{\text{det}}^{(n\Omega)}$ of the tip oscillation frequency Ω (typically in the range 30–300 kHz) in the detector photocurrent allows obtaining mainly a near-field response [38, 58, 59], eliminating the much stronger signals from scattering by the sample alone or by the tip alone.

In a heterodyne system [46], which is similar to the Mach–Zehnder interferometer (see Fig. 2), the light frequency in the reference beam is $\Delta = 80$ MHz shifted with respect to the light frequency ω in the laser beam (633 nm) being scattered by an ASNO tip. A lock-in detector is tuned to the combination frequency $\Delta + n\Omega$ to recover the photodiode signal. Keeping the homo- (hetero-)dyne recovery of the higher harmonic components in mind, we can rewrite expression (4) as

$$I_{\text{det}}^{(n\Omega)}(\mathbf{r}_{\text{tip}XY}) \sim E_{\text{loc}}(\mathbf{r}_{\text{tip}XY}) \alpha_{\text{eff}}^{(n\Omega)}(\varepsilon_s(\mathbf{r}_{\text{tip}XY})), \quad (6)$$

which involves only the amplitude of the local optical field E_{loc} over a surface point $\mathbf{r}_{\text{tip}XY}$ where the tip is located, and the averaged tip polarizability $\alpha_{\text{eff}}^{(n\Omega)}$ (depending on the parameters of the cantilever mechanical oscillation), which is mainly determined by the dielectric constant of the tip and the surface below it.

We note that the near-field component of the signal in a homodyning (heterodyning) system is a short pulse, whose duration is only 5–10% of the tip oscillation period (see Fig. 3). Thus, recovering just one single harmonic component $n\Omega$ means that some part of the useful signal is ignored. As a measure of the near-field fraction in the signal, it would be interesting to detect the whole area of the pulse that appears at the time of contact. Unfortunately, as the tip approaches the surface, not only the scattered wave amplitude but also its phase is modified [60]. In addition, the complex approach curve depends on the dielectric function of the tip and the surface, on the shape of the tip, and on the wavelength. In addition, the problem of the actual separation between the tip and the surface remains open in the TappingMode™ regime (the method assumes a ‘blind area’ between the sample and the lower dead point of the tip oscillations). Therefore, the problem of correct near-field component recovery in the optical response has not been properly solved yet.

It was reported in [61] that 18 higher harmonic components of the tip oscillation frequency were recorded in the photocurrent spectrum simultaneously, along with their amplitude and phase, using the tip-to-surface approach. The scanning head in the reported experiment was used in the TappingMode™ with the normal oscillation amplitude of 100 nm, and the Michelson setup was used for optical homodyning. It was shown that the approach curve is different for different harmonic components. The authors reconstructed the true approach curve (dependence of the photodetector signal on the tip-to-surface distance) from the amplitudes and phases of all separately measured harmonic

components in the photocurrent spectrum. A successful attempt to simultaneously use all higher harmonic components in signal acquisition is doubtless an achievement, but the question of “what the real tip–surface distance was in the experiment” was left without an answer in [61].

We note that the field amplitudes in (3) are complex quantities in a rigorous consideration. Therefore, the changes in the photocurrent caused by the tip oscillation depend on the phase difference between the reference beam wave and the wave scattered by the tip (see Fig. 3a). To obtain the true value of the near-field component, the measurement results must be averaged over all possible phases of the reference beam. In Keilmann’s heterodyning system [46], this is done automatically, because the acoustical–optical modulator shifts the optical frequency of the beam scattered in the first diffraction order by a running acoustic wave. The modulation frequency is $\Delta = 80$ MHz in [46], and therefore the reference beam phase makes a full turn over the tip-scattered wave phase 80 million times per second.

In the homodyning (Michelson-like) ASNO system, the reference beam phase should be modulated by the seesaw of the reference arm mirror. Under the assumption that interference of the signal and reference beams is ideal, only two positions of a reference mirror suffice, corresponding to a 90° phase difference between them [62]. Nevertheless, most ASNO users [56, 63–65] prefer moving the reference mirror smoothly (a minimum of a half-wavelength mirror stroke), to store the detected signal at several points, and finally to fit the interference (sinusoidal) curve in order to average over all reference phases.

In [63], the reference arm length is modulated by a sinusoidal law, and signal recovery is managed in a digital system by a complicated decomposition of the signal over the eigenfunctions of the problem. The mirror motion frequency was reported in [63] to be 200 Hz, which means a 5 ms acquisition time for a single raster point. In [65], the mirror oscillation frequency was 500 Hz.

Nevertheless, a sinusoidal law of phase modulation does not seem to be optimal from the measurement standpoint. In such a mode, the mirror spends most of the time near the motion dead centers, where its physical velocity is low. If an ADC runs at a constant sampling rate (recommended by hardware engineers), some values of the reference phase would be recorded too densely in the signal, while the contribution of other reference phases would become too small. The sawtooth law of the reference mirror motion (with smooth U-turns at its dead centers) implemented in [66] allows the two signal recovery operations to be separated. First, the peak caused by near-field interactions is recovered within a single period of tip oscillation (as a single higher harmonic or as the area of the pulse under the gate). Second, averaging over the reference phase is done on the array of first-stage results in order to recover the sinusoidal component of the signal response to the reference phase modulation. All ‘intermediate signals’ can also be shown by a virtual oscilloscope. Their visual control has shown, for example, that the motion law of a reference mirror differs from the expected ramp-like one.

Depending on the mirror mass, distortions with the piezo-stage PI S-316 occur at frequencies of 50–250 Hz. Thus, the acquisition time of a single point is limited by 4–20 ms. The ramp-like law of mirror motion used in [67] made it possible to connect the detector output (after recovering the second harmonic component in the optical signal) to the input of a conventional Fourier-transform IR (FTIR) spectrometer.

In [64, 68], constant-velocity motion of the reference beam mirror was used to store the signal dependence on the delay of the sample response to an ultrashort light pulse.

An improvement in optical hetero- and homodyning is also reported in [69]. To monitor the position of the reference arm mirror, an additional HeNe laser beam is used, directed parallel to the working beam. Such a trick was previously used in Fourier-transform spectroscopy instrument design. Interferometric direct measurement of the reference mirror position helps to stabilize the phase of the ASNOm signal stored at the working wavelength, while the precision of mirror position control is then determined by the wavelength 633 nm, instead of the 5 to 12 times longer wavelength used for measurements of the sample response.

2.4 Spectroscopy of elastic light scattering in an ASNOm

In the first papers investigating the spectral features of the near-field tip response, researchers changed the working line of a laser used to irradiate the probing tip and to detect the scattered wave by optical homodyning [42, 51, 64, 70–73]. With a coherent laser line, it was enough to move the reference mirror just a half-wavelength (a few micrometers). Spectroscopy with such a setup was limited, however, by the set of laser lines and by the width of the laser tuning band. Both are typically rather poor. The Michelson interferometer, which is typically present in an ASNOm system, can in principle be used to build a kind of conventional FTIR spectrometer by increasing the length of the reference mirror working stroke.

To calculate the scattering spectrum of a probing tip over the sample, the CPU of a conventional FTIR spectrometer can be used. Higher harmonic components of the tip oscillation frequency [67, 74] must be used as the input signal instead of the whole photodetector response. The spectral resolution of the instrument is then determined by the mirror working stroke in the reference arm. It must be some millimeters or even centimeters in length in order to compete with conventional FTIR spectrometers.

The capabilities of the ASNOm spectroscopy technique are limited by the low angular brightness of the thermal (blackbody) sources of radiation, which are in principle expected to be used as the light sources to irradiate the tip. Nevertheless, it was shown experimentally in [74] that the brightness of a glow bar suffices for a FTIR spectrometer to manage the quasihomodyning detection of light scattered by the tip. Another approach might be to use a synchrotron as a bright wide-band source [67]. A synchrotron and an FTIR spectrometer (Bruker) were successfully used with an ASNOm [67] to obtain the ‘absorption’ spectra of γ -globulin dried on an Si substrate and the spectra of peptoids (N-substituted glycines) on an Au substrate. The authors claim that the lines of Amide I, Amide II, and Amide III can be recognized in the spectra. A comparison to spectra obtained by conventional spectroscopy demonstrates almost no difference. For an ASNOm operation, the conclusion was reached that it is possible to use the libraries of spectra already collected by chemists and biologists.

3. Material contrast in ASNOm images

3.1 Approach curve dependence on the dielectric constant

A rather detailed consideration of the sSNOM signal dependence on the sample medium is contained in [40]. It is

mentioned in the paper that it is difficult to recover the value of the sample dielectric function under the tip from an ASNOm signal without ambiguity. The complex amplitude of a wave scattered by the tip [see, e.g., expression (2)] depends not solely on the dielectric function values of the tip and the sample under it. The shape of this approach curve is also determined by the distance between the surface and the tip apex. The dependence of the scattered wave amplitude on the gap is highly nonlinear, and therefore an error in the absolute value of the gap (tip height relative to the surface) can distort the calculation of an optical approach curve dramatically. In TappingMode™ feedback [57], where the amplitude of cantilever beam-driven oscillations is relatively large (50–150 nm), the changes in the tip oscillation phase or amplitude are measured as a feedback input signal. In small-amplitude (0.5–1 nm) feedback modes, the frequency [75] or the phase [76] shift of cantilever oscillations caused by the shape of the surface potential [77] is measured. We must keep in mind that the absolute position of the optical interface with respect to the tip location remains unknown in all these cases.

In systems using an STM sensor for topography feedback [24], the absolute position of the surface is known by the appearance of tunnel current. A disadvantage of the STM sensor is that only well-conducting substrates can be used for experiment. The jumping mode [78] is rather interesting for implementation in an ASNOm instrument. In such a mode, the approach–retract cycle of the tip is arranged at every point of the scanning raster, typically in a seesaw mode with a frequency of some kilohertz. In such a mode (also called HybridMode™ by NT-MDT), the tip comes into full contact with the sample at the bottom dead center of its motion, and this can be detected by a slight cantilever bend. Thus, HybridMode™ sensing of the tip–surface contact provides information on the absolute vertical position of the surface, and this advantageously differs from oscillatory modes in terms of an approach curve interpretation.

3.2 Mapping of semiconducting structures with an ASNOm of elastic scattering (sSNOM)

A signal collected by an ASNOm, as shown in expressions (4) and (5), is determined by the effective polarizability of the probing tip in the presence of a surface, and therefore by the surface dielectric function value at the probe location. The image of a bipolar transistor cleaved edge [41] in Fig. 4 was collected at a wavelength of 10.75 μm . An Si base chip, SiO₂ and Si₃N₄ insulators, and Al and W contact metals can easily be distinguished in the picture. It can be seen that the ASNOm provides the amplitude and phase of the tip scattering simultaneously, and therefore doubles the amount of information.

In this case, the ASNOm technique allows distinguishing not only different materials of a sample by their dielectric constant but also heavily doped (10^{20} cm^{-3}) regions of silicon from low-doped (10^{18} cm^{-3}) ones. Doping contrast (mainly present in the scattered wave phase) occurs because the plasma of free carriers contributes mainly to the imaginary part of the dielectric function value, while silicon itself has a purely real dielectric constant (Si is known to be transparent at the working wavelength 10.7 μm). Simulations based on the Drude model [79] demonstrate a perfect fit to the experimental data. The plasma frequency of the free-carrier subsystem crosses a laser line during the scanning (this frequency is below the laser line in low-doped regions of the surface and above the laser line in heavily doped regions),

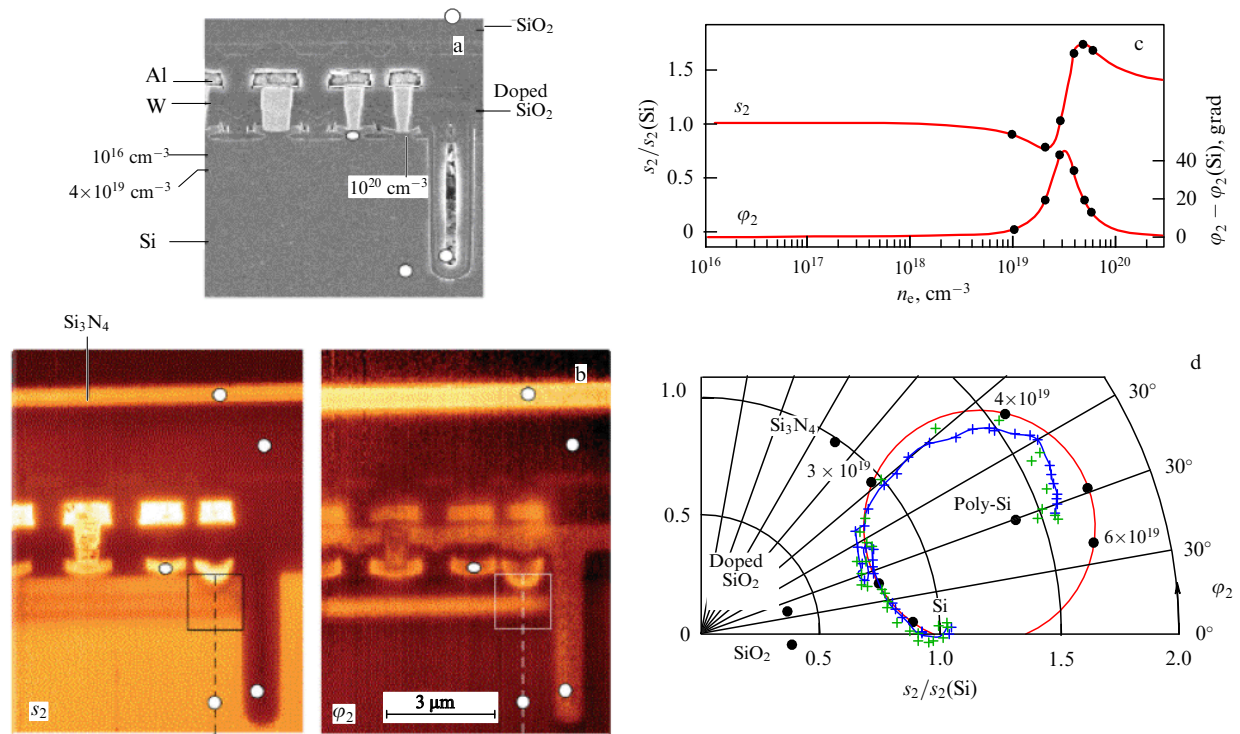


Figure 4. (Color online.) Cleaved-edge image of an Si chip containing a bipolar transistor. (a) Electron microscopic image, (b) amplitude and phase of the ASNOM signal recorded at a wavelength of $10.75\ \mu\text{m}$, (c) calculation of the amplitude and phase of the ASNOM signal at different concentrations of free carriers, (d) amplitude and phase along the section line on the maps in (b) plotted on the complex plane.

such that the set of signal values collected with an ASNOM forms a line close to the expected circle on the complex plane.

To estimate the optical spatial resolution of the instrument, the authors of [41] considered an image of an Si_3N_4 layer nominally 10 nm in thickness. The ASNOM image has a width of 40 nm, and this was claimed to be the optical resolution of the instrument.

Images of Si_3N_4 nanocrystallites located on an Si substrate also demonstrate the ability of an ASNOM to distinguish semiconductors [71]. It can be seen in the paper that an ASNOM signal (which is literally the *nonlinearity of a scattered wave amplitude dependence on the tip-sample distance detected as the second harmonic component of the tip oscillating frequency*) reflects the spectral properties of an object under the tip in a slightly unusual way. With any line of a tunable CO_2 laser used as a coherent light source in the experiment, the optical signal collected over an Si_3N_4 particle was divided by the complex value of the signal collected over the Si substrate. Silicon is transparent in this spectral band, and hence its response can be assumed to be a reference value. Spectra calculated in such a way contain peaks corresponding to the spectra of Si_3N_4 particles known from conventional spectroscopy, but mainly in the phase of an ASNOM signal, not in its amplitude.

To explain the spectra obtained in the experiment, and to compare the results with spectra collected by conventional spectroscopy (e.g., in [80, 81]), the authors made rather detailed and rigorous calculations [25]. The tip was assumed to be a spheroid [39], and its electrostatic image on the surface was considered [37, 38]. A substrate was also included in the model, in addition to the tip and nanoobject being investigated, and the finite height of all crystallites was also taken into account. Finally, a rather good fit was achieved between theoretical simulations and experimental data, and thus a

complex value of the ASNOM signal was reasonably explained.

Images of InGaN crystallites grown on a GaN substrate were presented in [82]. Additional factors were considered in the paper (vertical displacement of the tip enveloping a crystallite, tip-object electromagnetic interaction at intermediate distances in the near dipole zone), which may cause some distortions in the images being obtained. Boron nitride nanotube images collected at different wavelengths corresponding to different modes of lattice oscillations were reported in [83]. Contrast images of boron nitride nanotubes were also obtained in [61]. At light frequencies corresponding to the surface phonon polaritons, the image contrast is significantly higher than at frequencies outside the polariton resonance band.

The performance of an ASNOM in the terahertz band [84] was demonstrated by Keilmann's group in a self-made system with a tungsten tip with an apex radius of 200–300 nm. All tests typical for an ASNOM experiment were carried out to convince the researchers that the signal collected with an instrument is in fact caused by the near-field interaction between the probe and the sample surface. An approach curve was acquired. The tip vertical position at which the noticeable signal arises was reported as 50–70 nm at a working frequency of about 1 THz (wavelength of about $300\ \mu\text{m}$).

In another paper [85], a semiconductor transistor structure (with the sample also prepared by the cleaved edge technique) was mapped with an ASNOM simultaneously in the mid-IR and THz bands. The image obtained at a frequency of 2.54 THz (Fig. 5) corresponds, in general, to an image obtained with a CO_2 laser at a light frequency of 28 THz. It was shown that this method allows mapping the surface response with a lateral resolution of about 40 nm and

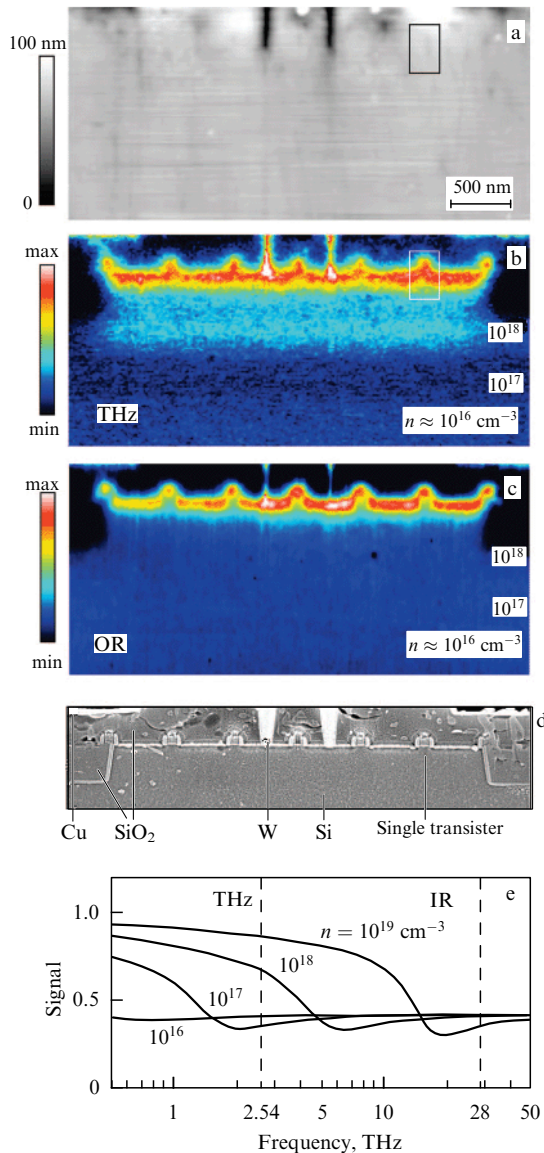


Figure 5. Cleaved-edge images of an Si structure containing transistors: (a) topographic AFM image, (b) amplitude of the collected ASNM signal at a frequency of 2.54 THz (wavelength about 120 μm), (c) amplitude of the ASNM signal collected using a CO_2 laser at a wavelength of 10.7 μm , (d) image obtained with a scanning electron microscope, (e) calculated frequency dependence of the ASNM signal collected over the surface of an Si sample at various n -doping concentrations [85].

provides an image contrast not only between different materials but also between different doping regions of the same silicon.

The terahertz band was also used in an ASNM to investigate VO_2 films on a sapphire substrate [86]. Detection of a local plasmon response under the tip made it possible to observe the formation of metal islands caused by a metal–insulator phase transition. VO_2 strips 3–100 μm in length were formed on a sapphire substrate from one Cr/Au contact pad to another. Voltage was applied between these contact pads, and under some voltage (150–170 V, depending on the temperature and VO_2 strip length), VO_2 becomes conducting, judging by the macroscopic measurements of electric current. The appearance of free carriers in the VO_2 strip causes a plasmonic term in the expression for the film dielectric constant to appear, which, in accordance with (2), changes

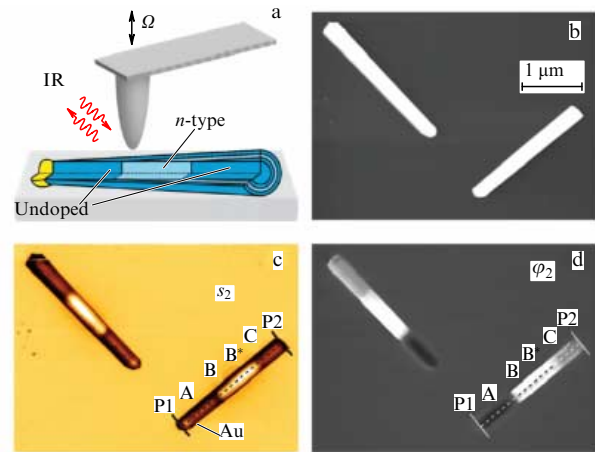


Figure 6. (a) Image of a nanocrystallite InP of a cylindrical shape (nanowire) obtained with (b) an electron microscope, (c) ASNM amplitude, and (d) phase maps at a wavelength of 11.2 μm [87].

the response of the CuBe tip attached to the sample top. The tip radius was about 1 μm , sufficient to achieve a subwavelength lateral resolution, which allowed the authors to conclude that a metal phase formation occurs on the VO_2 film by islands. We have the impression, however, that there was no raster scanning in the experiment reported, because there is no ASNM map of the sample in that paper (in our opinion, such a map would have been a valuable addendum to the paper).

The doping level, which varies along the InP nanocrystallite with an elongated shape, was measured in [87] with an ASNM (Fig. 6) at a laser wavelength of 11.2 μm (the 893 cm^{-1} line of a $^{13}\text{C}^{16}\text{O}_2$ laser). As can be seen, the doping level can be easily distinguished in the ASNM pictures, but is hardly visible in the scanning electron microscopy images.

A map of the optical response was also obtained in [88] for the domain structure on a ferroelectric surface. As reported in [89], an ASNM providing local optical spectroscopy made it possible to detect the coexistence of Li_xFePO_4 and FePO_4 crystalline phases in Li_xFePO_4 microcrystals that are depleted in lithium.

Epitaxially grown islands of InGaN were mapped with an ASNM [90] at various wavelengths. Islands were formed in the 3D growth mode on a sapphire substrate with a GaN buffer layer. The authors discuss possible reasons why two ASNM images of the same surface area acquired at wavelengths of 532 and 633 nm do not fit each other. One of the explanations is that the surface consists of relatively large (100–300 nm) grains, comparable in size to the tip itself. Under such conditions, enhancement of a local field and therefore enhancement of the tip–sample interaction can happen not exactly at the tip apex. In that case, there can be wavelength-dependent variations in the amplitude of the light wave scattered by the probe and obtained with an ASNM.

Semiconductor structures and, occasionally, biological samples require a low temperature for investigations, and many authors have reported on the design of a low-temperature ASNM. The instrument geometry reported in [91] is not the best solution in our view. The light from an objective irradiates the tip from a direction along the tip shaft, and therefore the interaction of the light electromagnetic field with dipole oscillations in the tip is not optimal. In another design [92], the light arrives to the tip at an angle to the tip

axis, and one can therefore expect a much better coincidence between the **E** vector in the irradiating wave and the direction of dipole oscillations in the probe.

3.3 sSNOM imaging of biological objects

Naturally, the use of ASNOMs is not limited to investigations of the response of semiconductor samples. On the contrary, most images have been obtained by the developers of the method in order to attract the attention of biologists and chemists. In one of the first studies [15] devoted to ASNOMs, the authors, following the tradition established by the inventors of the scanning electron microscope, presented the image of a tobacco mosaic virus, obtained at a wavelengths of 633 nm (HeNe laser) and 514 nm (Ar⁺ laser). The tobacco mosaic virus image, in that case taken in the mid-IR range, was published [93] by Keilmann's team. The authors did not confine themselves to taking an image. They claim that the images obtained at different lines of a tunable CO₂ laser allow identifying the Amide-II absorption band (which corresponds to the C = O vibrational mode in the amide group with a characteristic frequency of 1650 cm⁻¹). Moreover, the images show that the amide group is located in the virus envelope. The spectral history obtained at different lines of tunable CO₂ lasers (modified to work in the 6 μm band instead of the conventional 10.6 μm band) is also presented in [93]. The raster points from which the spectral response was taken to build a 'spectral history' set are located on a straight line across the virus body. Similarly, the emergence and disappearance of the IR vibrational Amide-I line in the ASNOM image was demonstrated in [72] on a purple membrane.

ASNOM imaging and spectroscopy of protein complexes (tobacco mosaic virus, ferritin complexes, insulin aggregates, *E.coli* membrane) were reported in [73]. A tunable quantum cascade laser was used as a source of coherent radiation. It follows that (a) surface mapping obtained at one selected wavelength and (b) spectroscopy obtained at one selected point are different modes of operation. Acquiring a tobacco mosaic spectrum required 22 min in [73], which means that ASNOM scanning of a surface with a simultaneous spectroscopy at each raster point would take an unacceptable length of time.

3.4 ASNOM imaging of polymers

Contrast ASNOM images of polymers have also been demonstrated in many papers (see, e.g., [73]). In [73] (Fig. 7), a quantum-cascade laser (QCL) is used as a tunable radiation source, a Michelson interferometer with a modulated reference phase is used for optical homodyning, and the near-field component in the photocurrent is recovered at the third harmonic component of the tip oscillation frequency. In a co-polymer of polystyrene (PS) and polymethyl-metacrylat (PMMA), areas of different chemical compositions are easily distinguished with a lateral resolution of 20–40 nm.

Similar results were obtained earlier in [94], also at the optical frequencies of 1650–1800 cm⁻¹, with the only difference that the impregnations of PS balls look more regular. A PMMA layer 90 nm in thickness can be well distinguished on an Si surface [70]. In that work, an attempt was made to identify the PMMA by characteristic absorption lines of C–O–O, CH₂, and C = O groups.

3.5 Undersurface imaging of 'buried' objects

The ASNOM operational principle is to use a change in the tip optical polarizability caused by the presence of a sample

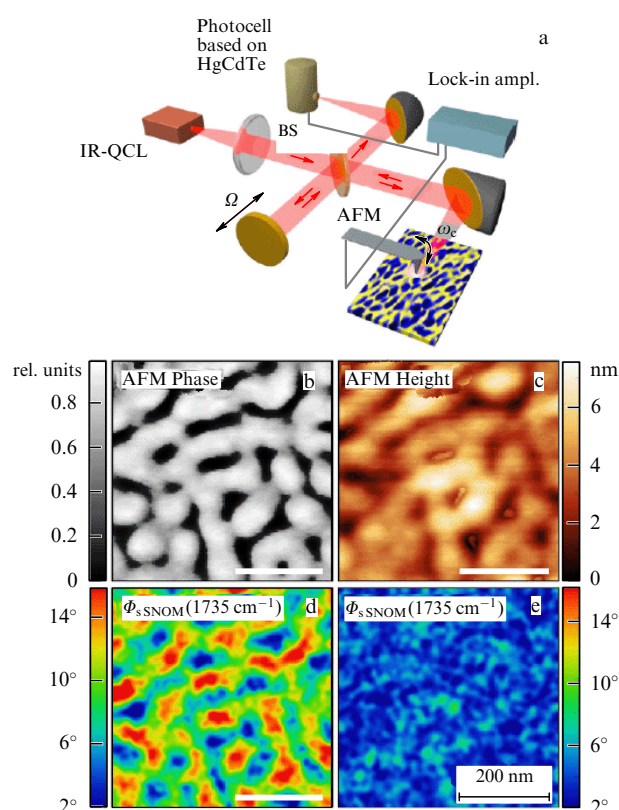


Figure 7. (Color online.) (a) Setup configuration and (b–e) images of the PS-b-PMMA copolymer surface. The beam of a QCL is partially reflected by the beamsplitter into the reference arm of a Michelson setup, whose length is modulated by the periodic motion of the mirror along its axis. Reflected back, the reference beam hits the photodetector. Another part of the laser beam is focused by the mirror objective onto the probe in the AFM-like ASNOM scanning head. The light scattered by the probe passes back through the objective and, reflected from the beamsplitter, also hits the detector. A lock-in recovers variations in the photocurrent at the higher harmonic of the frequency of normal tip oscillations. (b) Phase of mechanical vibrations of a cantilever. (c) Surface topography. Optical phase of the ASNOM signal (d) at resonance and (e) outside the resonance with the carbonyl vibrational mode in PMMA [65].

surface. The amplitude and phase of the driven dipole oscillations in the tip can also be modified by objects 'buried' in the sample at a depth of the system characteristic dimension, the tip radius. A sharp image was obtained in [45] for Au islands covered by a PS layer. It is not surprising that a graphene layer with its thickness of a few atoms allows distinguishing [95] a submerged boundary of an SiO₂ layer formed on an Si substrate (Fig. 8).

Maps of a graphene sample (Fig. 9) containing single-layer, double-layer, and triple-layer thick fragments of a graphene film on an Si substrate, which is isolated from graphene by an SiO₂ layer, are obtained (at different bias voltages of graphene with respect to the substrate) in [96]. It is shown in that paper that *bilayer* and *double-layer* graphene flakes could be distinguished in ASNOM maps. These flakes (in the opinion of the authors) differ by the geometry of stacking the crystalline layers. If a medium has some special features in its refractive index (for example, a band of negative values of the permittivity at optical frequencies close to the SiC lattice resonance), the medium layer covering the objects to be imaged can introduce complex distortions into the image, which the authors (by analogy with optical metamaterials) call 'superlensing' in their paper.

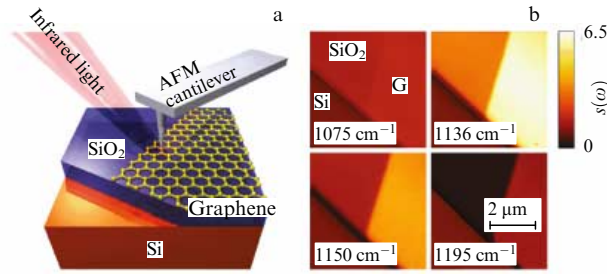


Figure 8. (a) Experiment geometry and (b) ASNM signal amplitude map of a graphene film located on an Si substrate coated with 300 nm SiO₂. ASNM maps are collected at different wavelengths [95].

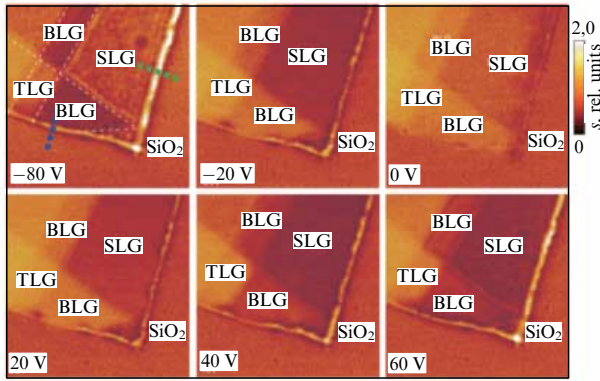


Figure 9. (Color online.) ASNM amplitude map of the signal obtained by scanning a graphene film containing areas of different graphene thicknesses. The wavelength is 11.33 μm. The images were taken at different bias voltages applied to a graphene film with respect to an Si substrate. This gate voltage shifts the Fermi level in graphene and thus modifies the electron mass in the graphene layer [96]. The notation used is as follows: SLG, single-layer graphene; BLG, bilayer graphene, TLG, triple-layer graphene.

3.6 Visualization of surface polariton waves

As can be seen from expression (4) for the amplitude $E_{\text{scatt}}(\infty)$ of the wave scattered by the tip, this amplitude is proportional to the effective tip polarizability $\alpha_{\text{eff}}(r_{\text{tip}Z}, \epsilon_s(\mathbf{r}_{\text{tip}XY}))$ times the amplitude of the local electromagnetic field $E_{\text{loc}}(\mathbf{r}_{\text{tip}XY})$ at the point of the tip location. In experiments related to material contrast, it is usually assumed that the local light field amplitude E_{loc} is the same over any point of the surface, being determined by the electromagnetic field in the laser beam focused on the tip. Under that assumption, all changes in a detected ASNM signal are attributed to the sample dielectric function $\epsilon_s(\mathbf{r}_{\text{tip}XY})$, assuming, more or less reasonably, mechanical oscillations of the cantilever to be constant. But the local electromagnetic field above the sample surface is not always homogeneous. It can be distorted by objects located on the surface (for example, by metal contact traces on a semiconductor structure) or may even get under the tip as a surface wave excited by pump radiation on entirely different areas of the surface.

An image of the $E_{\text{loc}}(\mathbf{r}_{\text{tip}XY})$ normal component distribution over a crystalline SiC surface in a running phonon–polariton surface wave in the frequency band 880–940 cm^{−1}, which corresponds to an SiC lattice resonance, was obtained in [98] (Fig. 10). In that particular case, as was shown in [56], the ASNM signal is, due to a lucky combination of problem parameters, proportional as a complex number to the amplitude of the local light field. The focal spot of the laser

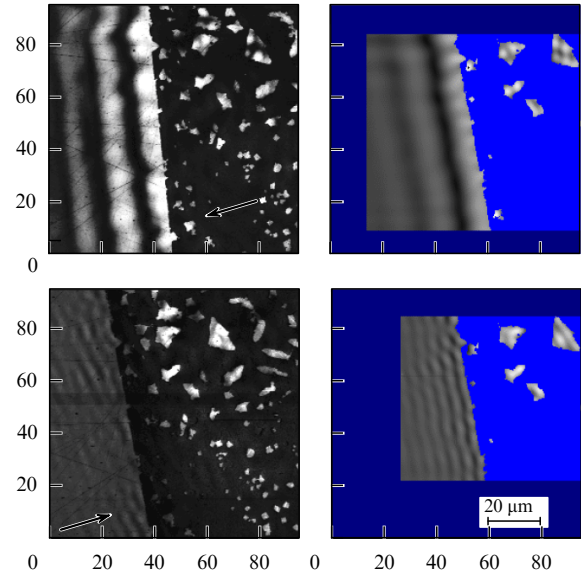


Figure 10. Experimentally mapped (left) and simulated (right) distributions of the amplitude of a surface phonon–polariton wave excited on an SiC crystal surface by a plane wave from a CO₂ laser with different directions of the exciting light wave (shown by arrows) [98].

beam that irradiates the area around the probing tip was made quite wide (100–120 μm). Test measurements consisting of focal spot 2D scanning around the fixed tip location (see Fig. 6 in [99]) have proved that the pump beam phase is described by the same wave vector $\varphi(x, y) = \mathbf{k}_{\text{las}} \mathbf{r}_{xy}$ within the whole focal spot. Therefore, we can expect the whole sample surface around the probe in Fig. 10 to be irradiated by a monochromatic plane wave. Part of the crystalline SiC surface was covered by a metal mask opaque to pump radiation. On the open areas of the SiC sample, the plane wave of driving radiation excites running and standing phonon–polariton waves. The dispersion law of these waves [100]

$$k_{xy}(\omega) = \frac{\omega}{c} \sqrt{\frac{\epsilon_{\text{vac}} \epsilon_{\text{SiC}}(\omega)}{\epsilon_{\text{vac}} + \epsilon_{\text{SiC}}(\omega)}}, \quad \epsilon_{\text{vac}} \equiv 1, \quad (7)$$

fully corresponds to expectations [101–103] based on the SiC constants [104, 105] used to calculate the dielectric function of SiC:

$$\epsilon_{\text{SiC}}(\omega) = \epsilon_{\text{SiC}}(\infty) \left(1 + \frac{\omega_L^2 + \omega_T^2}{\omega_T^2 - \omega^2 - i\omega\Gamma} \right), \quad (8)$$

where ω_L and ω_T are the longitudinal and transverse phonon mode frequencies, which are experimentally known, and $\epsilon_{\text{SiC}}(\infty)$ SiC is the dielectric function value at frequencies much higher than the lattice resonance frequency. The amplitude and lateral period of the polariton waves excited in the coinciding or counter-propagation geometry of the pump radiation are similar to the SNOM maps obtained for plasmonic waves [106].

A metal mask opaque to radiation contains arbitrarily shaped openings 5–10 μm in size. These features leave an SiC crystal surface open to pump radiation as well as ASNM probing. These areas can be regarded as small 2D particles in the experiment. It was found that the light field amplitude in phonon–polariton waves excited with a laser and measured

with an ASNOM over such ‘lakes’ is several times higher than the field amplitude of a running phonon–polariton wave on an infinite open surface of SiC excited and measured in the same geometry. An enhancement of the local field in the 3D case was previously observed in [107]. This effect is similar to plasmonic resonance in small metal particles (incidentally, mathematical expressions that describe phonon and plasmon surface polaritons are almost the same).

The distribution of the field amplitude measured by an ASNOM over open SiC areas (see Fig. 10) is in excellent agreement with calculations done by integrating the Green’s function over all the illuminated areas of the surface. The signal $I(x, y)$ collected by an interferometer detector for a tip position (x, y) on the surface plane can be expressed in terms of complex numbers as

$$I(x, y) = E_{\text{las}}^*(x, y) \left(\alpha_{\text{tip}} E_{\text{las}}(x, y) + \alpha_{\text{tip}} \xi \times \int_{XY} E_{\text{las}}(x', y') G(x - x', y - y') dx' dy' \right), \quad (9)$$

where the term $E_{\text{las}}(x, y) = E_0 \exp(i\omega t + i\mathbf{k}_{\text{las}} \mathbf{r}_{xy})$ describes the field of driving radiation at a tip location point (x, y) , delivered there directly as a laser beam with the wave vector projection \mathbf{k}_{las} onto the sample plane. The integral, in turn, describes all surface phonon–polariton waves excited by a laser beam at other points (x', y') on the sample surface and then delivered to the tip location (x, y) as divergent surface waves. The complex factor ξ is used to recalculate the subsurface local field in the running phonon–polariton wave into the local field above the surface, which excites dipole oscillations in an sSNOM probe. The notation XY at the integral denotes all points of the surface uncovered by the metal mask from which a polariton wave can propagate toward the tip. A complex Hankel function $H_0(k_{xy}(\omega) \Delta R_{xy})$ with the parameter $k_{xy}(\omega)$ equal to an eigenfunction of homogeneous problem (7) was used as the Green’s function. Because the wave equation is linear, the sum of homogeneous problem solutions must also be a solution.

An ASNOM image [108] of a phonon–polariton wave excited on an SiC surface in the presence of a round Au island by external coherent radiation at the frequency of the SiC lattice resonance can also be described well by Green’s function integration. A horseshoe metal mask formed on an SiC surface becomes a source of a converging surface wave [109] that can be used in developing surface optics devices similar to those in the optics of surface plasmon waves [110].

Excitation and propagation of running phonon–polariton waves (with the wavelength 7–7.25 μm) in boron nitride nanotubes fixed on a gold substrate were investigated in [111]. The dispersion law was plotted experimentally. The role of the substrate roughness in the excitation of running (standing) waves in such a one-dimensional structure has been noted. An interaction between longitudinal and transverse modes of phonon vibrations in a boron nitride nanotube was investigated with an ASNOM in [112]. In contrast to typical applications of ASNOMs, in this experiment an ASNOM was used to irradiate the probing tip simultaneously with two lasers (at frequencies of the longitudinal and transverse phonon resonances), and the optical response obtained at one wavelength feels the influence of the other.

An ASNOM was used to acquire maps of the electromagnetic field distribution in surface waves in plasmonic

structures. Plasmonic states were excited in the visible wavelength band (695–1250 nm) in Au nanodisks 200–300 nm in diameter formed on a glass substrate. A very elegant experimental trick was used to collect the images. To excite the structures, s-polarized light with the \mathbf{E} vector parallel to the surface was used to irradiate the sample, while the radiation scattered by the probing tip above the disk was collected in p-polarization, with the \mathbf{E} vector normal to the surface plane. The metallized probe tip had a characteristic size of 5–10 μm (more than 10 times larger than the Au disks being investigated) and its direct response to a p-polarized pump wave would be much stronger than the electromagnetic response of the disks to be re-emitted by the tip.

Maps of plasmon–polariton waves excited in Au dipole nanoantennas of various sizes and shapes were obtained in [113]. Plasmonic response of elements of a Yagi-Uda antenna at a light wavelength of 1064 nm was investigated in [114]. Similar measurements, but at a 9 μm wavelength, were reported in [115]. In that paper, the sample was also irradiated from a substrate bottom to provide pump polarization with the \mathbf{E} vector parallel to the sample plane.

Nevertheless, maps of the \mathbf{E} -field distribution in a running *plasmon*–polariton wave collected with a metal-coated tip using SNOM should be considered with some doubt. The focus of measurements in an ASNOM is higher harmonic components of the tip oscillation frequency contained in the photocurrent signal of a detector mounted at the interferometer output. As can be seen from the simplest model, “a nanometer-size ball (tip) over a flat surface (sample)” expressed by (3), the amplitude of light scattered by the tip depends on the local field $E_{\text{loc}}(\mathbf{r}_{\text{tip}})$ at the tip location, and, in particular, on the tip height $r_{\text{tip}z}$ above the surface. The amplitude in a running surface *plasmon*–polariton wave decays exponentially in the normal direction, with a characteristic scale less than the wavelength. With the tip vibration span of 150–200 nm, the nonlinearity of the field amplitude dependence on the tip position plays a significant role even without any ‘electromagnetic contact’ between the tip and the surface. Higher harmonic components appear in the photocurrent just because the probe moves vertically from the area of a strong light field to that of a weak field. In such a case, the lateral optical resolution is no longer determined by the size of the contact patch between the tip and the sample.

Investigating surface *phonon*–polariton waves, with their decay scale equal to a few micrometers in the normal direction due to a larger characteristic wavelength, we can assume that the vertical (normal) oscillations of the tip do not significantly affect the light field amplitude that drives the tip dipole. An interpretation of the map images in the case of plasmon wave observation becomes even more complex. Keeping in mind the (large) dimensions of the probe and (small) dimensions of the object, and also the plasmonic nature of electromagnetic excitation in both of them, the signal being measured in an ASNOM is “plasmonic states in a probe slightly disturbed by the object” instead of the expected “plasmonic states in an object slightly disturbed by the probe.”

Although the published results principally agree with expectations based on theoretical calculations and far-field measurements, the field distribution measured by an ASNOM differs from the real one, and the resonances on the structures are significantly (by 20–30%) shifted in the wavelength or disappear entirely. In that sense, *phonon*–polariton surface waves are preferable as an object of

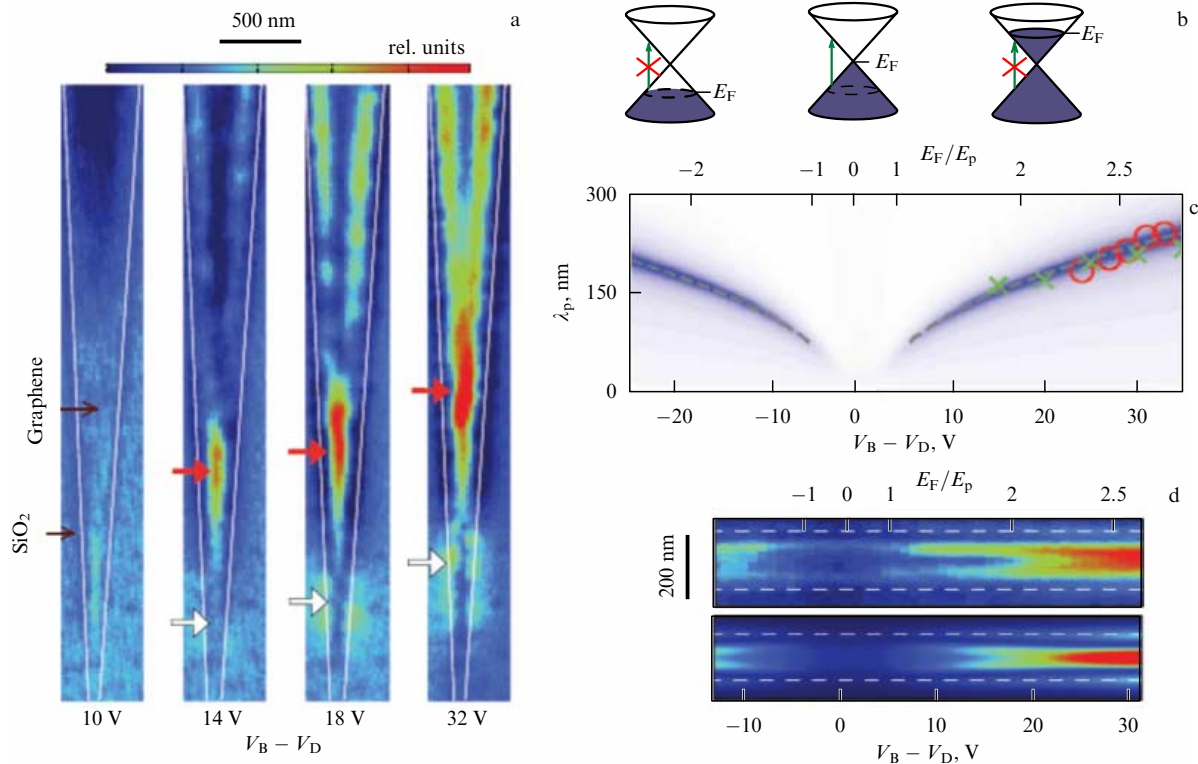


Figure 11. (Color online.) (a) ASNM response map (at the wavelength 11.06 μm) of a graphene wedge on the surface of an Si/SiO₂ substrate at different substrate potentials. (b) Filling of zones in graphene depending on the substrate potential. (c) Dependence of the resonance wavelength of a plasmon–polariton wave on the potential of the substrate, taking the contributions of interband and intraband transitions to plasmon decay into account (see Fig. 11b). (d) ASNM image of a 200 nm wide graphene strip in its dependence on the substrate potential, observed experimentally at the 10.7 μm wavelength (top) and simulated theoretically (bottom) in that case [117].

investigation. The sizes of sample areas and the number of carriers involved in the propagation of a surface polariton wave are much larger than the dimensions of a metal tip, and, in addition, the lattice centers oscillate under their resonance conditions, in contrast to the electrons of the tip metal.

A nanotube of boron nitride was used as a sample in [61]. It was shown in this example that a signal of higher harmonic components of the cantilever oscillation frequency detected in the photocurrent greatly depends on the spatial decay of the local electromagnetic field amplitude. In general, such a statement does not raise any objections. The landing curves presented in the paper are rather convincing. However, the use of an object 100 nm in size, much smaller than the probe (3–10 μm), as a proof of that statement is arguably doubtful.

To reduce the distortions introduced into the plasmon oscillations of a small (100 nm) gold coin with a huge probing tip (10–15 μm), the probe in [116] was made of a fullerene nanotube. This successful pioneering (2003) work made it possible to measure the amplitude and phase distribution of plasmon oscillations over a gold disk excited by an HeNe laser wave. However, judging by the fact that the nanodisk is mentioned in the text as just a point-like dipole, the authors were not impressed with the results of comparing their measured distribution of fields over the structure with those of theoretical calculations.

Plasmon waves have also been observed with an ASNM on graphene structures. A dispersion law of surface plasmon waves on graphene was obtained in [95]. In [117], a graphene flake was placed on an Si substrate covered with an SiO₂ isolating layer. The substrate was used as a gate in an FET,

and the bias voltage applied to it allowed shifting the Fermi level in the graphene and thus modifying the mass of electrically active carriers (Fig. 11). The shift of the plasma frequency and the dispersion law of plasmon–polariton waves caused by this were observed from the shift of the resonance point in a two-dimensional Fabry–Perot interferometer formed by a long narrow graphene wedge (with the opening angle of about 8°). ‘Gate bias’ was also applied to the substrate lying under a graphene flake in [96, 117, 118], and this also led to a change in the dispersion law for plasmon–polariton waves observed with an ASNM.

Plasmon–polariton waves were also excited in Ref. [119] by external monochromatic radiation incident on a graphene wedge (the wavelength of 10.8 μm used corresponds to one of the CO₂ laser lines). This wedge had an opening angle of about 15°, and the graphene thickness was double-layer (within 1 μm from the cusp) or single-layer (farther away). In the image presented, an increase in the standing wave amplitude is clearly seen for the width of the wedge that corresponds to a Fabry–Perot resonance. The paper is mainly devoted to the reflection of polariton waves on a film edge and crystal grain boundaries, which are also well distinguished in the ASNM amplitude and phase images.

The peculiarities of the electron spectrum of graphene that arise from the periodic modulation of atom positions in the crystal lattice are discussed in [120]. If a graphene film is mounted on top of a hexagonal boron nitride lattice (having almost the same lattice constant), the carbon atoms in the graphene lattice form a moiré pattern, due to the incomplete matching of the lattice period, and this leads to the appearance of a miniband.

4. Ultrashort light pulses

Among methods in which the interference of light scattered by a probing tip with a pump light beam is used to detect the signal, the use of ultrashort laser pulses is especially important. A Michelson interferometer equipped with parts that allow the modulation of the length of a reference arm suggest an idea to change the time delay of a short laser pulse in the detecting system.

In Ref. [68], an optical parametric oscillator (OPO) was used, pumped with Ti:Sa laser pulses ($\tau = 200$ fs and $\lambda = 5\text{--}8$ μm). The correlation dependences of the signal on the delay time of the reference pulse allowed obtaining the tip scattering spectrum by a Fourier transformation. A significantly long decay was observed in the optical polarization of an Au cluster located on a PTFE (teflon) substrate near an edge of an Au film. Such a cluster was, unlike its neighbors, optically coupled to the neighboring large film in an optimal way, and plasmon oscillation energy could therefore be transferred from the cluster to the metal film and vice versa.

The spectrum of a pumping laser ($\nu = 1100\text{--}1300$ cm^{-1}) covers the PTFE absorption lines $\nu_1 = 1160$ cm^{-1} (symmetric stretch of the C–F bond) and $\nu_2 = 1220$ cm^{-1} (antisymmetric stretch). The spectra were plotted corresponding to different delays of a homodyne reference pulse (to build the spectra, 200 fs fragments of the entire correlation curve were used). It was shown that for those clusters of gold that are optimally connected to the electromagnetic air by an ASNOM tip (which in this case acts as a rod antenna), the dephasing time T_2 of the ν_1 mode vibration in the PTFE substrate below them decreases from the usual 680 fs to 610 fs. It is mentioned in [68] that a decrease in the dephasing time of molecular vibrations correlates, in general, with the improvement in the electromagnetic matching between the sample and the external radiation provided by the ASNOM tip.

Ultrashort light pulses (pump pulse: $\tau = 100$ fs and $\lambda = 1.56$ μm ; probing pulse: $\tau = 100$ fs and $\lambda = 8.3\text{--}14.3$ μm) were used in [121] to investigate graphene samples on an SiO_2 substrate. The spectra of the tip response to a probing pulse were stored on a 300 nm thick SiO_2 layer and then normalized to the spectral response of Si, which is known to be transparent in this spectral range and can therefore be used as a reference. The spectral response of an ASNOM contains the SiO_2 lattice vibration lines $\nu_\alpha = 1125$ cm^{-1} and $\nu_\beta = 785$ cm^{-1} . After that, a graphene film was placed on the surface, and the ASNOM spectral response was acquired on such a sample. In most cases, the spectrum repeats the scattering spectrum of an empty SiO_2 substrate due to the vanishingly small thickness of the graphene film, and the difference between these two signals was used in further considerations. It is shown that such a difference spectrum depends on the presence of free carriers in graphene. The contribution of the ‘hot’ carriers produced by the pump pulse at 1.56 μm can be separated from the contribution of ‘cold’ carriers, whose concentration was changed by shifting the Fermi level in graphene and applying a bias voltage to the ‘gate’ (conductive Si substrate separated from graphene with an SiO_2 isolating layer).

The effect of lattice vibrations of SiO_2 on the dispersion law of Dirac carriers in graphene has been considered. The weight of the Drude term in the dielectric function of graphene, which depends on the carrier concentration, describes the reflection spectra of graphene satisfactorily. It is shown that the cooling of the carrier plasma lasts 1–2 ps, the

relaxation time being different for one-, two-, and three-monolayer thick graphene flakes.

The cooling of a free carrier plasma and, accordingly, changes in the plasmon properties of an InP sample, were investigated with an ASNOM in [122]. The pumping energy quantum ($\lambda = 1.56$ μm) was sufficient to excite interband transitions in InAs and therefore to create hot carrier plasma in a semiconductor. The ASNOM tip was irradiated with the probe light pulse ($\nu_{\text{probe}} = 600\text{--}2200$ cm^{-1}) of a variable delay. The tip scattering spectrum contains a free-carrier plasma response as broad peaks with a maximum at the frequency $\nu = 600\text{--}900$ cm^{-1} . The spectral position of this maximum depends on the pumping pulse energy, while the plasma frequency depends on the carrier concentration. The pulse duration of both lasers was 200 fs. Varying the probe pulse delay within 30 ps allowed calculating the plasma frequency and reflection coefficient dependence on time (both parameters recovered in the experiment demonstrate a sum of two exponentially decaying signals with the time constants 1 ps and 64 ps).

5. Spectroscopy with an ASNOM

In the foregoing, we mostly discussed those papers in which light scattered by an ASNOM tip was detected at the wavelength of the driving light source (including tunable sources). In those cases, optical homo- and heterodyning allows a significant increase in the detector sensitivity due to interference of a wave scattered by the ASNOM tip with a relatively strong wave of a reference beam. The ASNOM, as an instrument, is also applicable to other types of optical measurements, namely, the spectroscopy of luminescence and Raman scattering [123–130]. A probing tip acting as a micro-antenna and having a rather small contact patch provides quite effective coupling between the wave fields incident from outside and/or emitted to the space and the nano-object located on the sample surface.

5.1 Tip-enhanced Raman scattering (TERS)

The amplitude of the light field applied by an ASNOM probe to an object located on a surface straight beneath the tip is several orders of magnitude higher than that of a conventional light wave used to irradiate the tip and the sample. Hence, the efficiency rate of Raman scattering can be several orders of magnitude higher in an ASNOM than in conventional Raman experiments. One of the first TERS papers [131] reports the acquisition of a Rhodamine-6G spectrum with an ASNOM system. To enhance the signal to be collected, the authors also used a thin silver island film as a substrate, keeping the surface-enhanced Raman scattering effect (SERS) in mind. The irradiating light was directed by a high-NA objective from the bottom side of the substrate. As a result, a significant enhancement of the collected signal in the presence of an Ag-coated silicon cantilever-based tip was demonstrated. The tip radius was reported to be 40 nm in that case.

A similar approach (nonoptimal, as was found later) to irradiate a sample was used in [132] with an aperture-defined ASNOM (tapered fiber glued onto a tuning fork). The authors focused a laser beam ($\lambda = 488$ nm) onto a substrate from its bottom, and they also hoped for SERS with respect to additional signal enhancement. Nevertheless, the capability of an ASNOM to obtain the Raman spectra of a Brilliant Cresyl Blue dye was demonstrated, and the spectra vanished

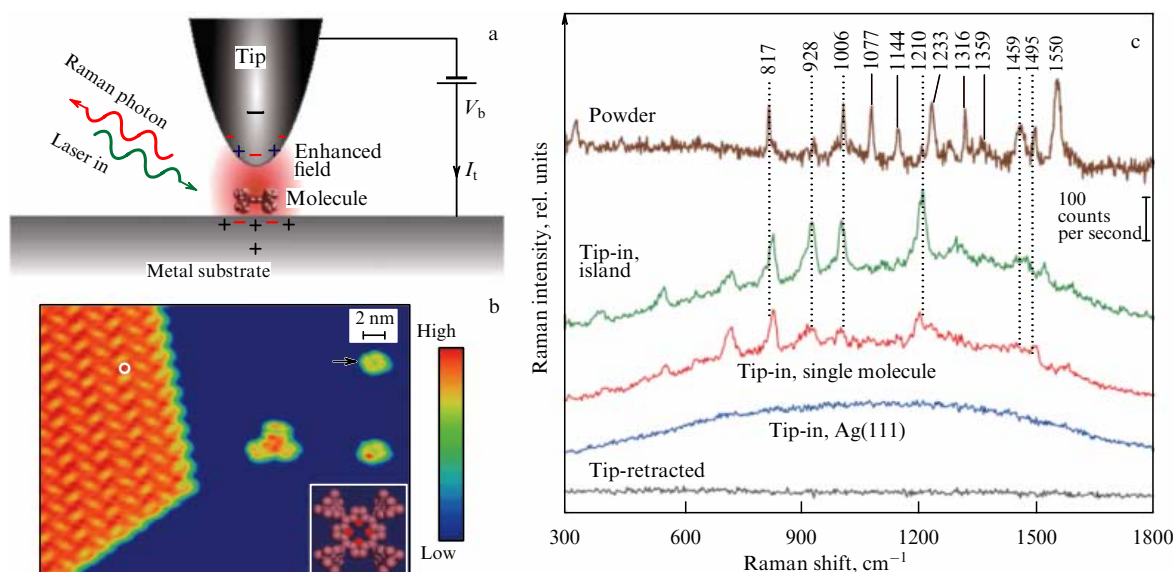


Figure 12. (a) Experimental setup, (b) STM topography map of submonolayered meso-tetrakis (3,5-di-tertiarybutylphenyl)-porphyrin (H2TBPP) molecules on Ag(111) obtained in the STM mode. (c) TERS spectra acquired at different points of a sample: on an island of H2TBPP molecules, on a single molecule, and on an Ag(111) substrate. Spectra were acquired at 120 mV, 500 pA, 3 s. To compare, the spectra acquired with the tip retracted 5 nm from the surface and the conventional Raman spectra of an H2TBPP powder are shown [137].

on tip retraction. TERS spectra of C_{60} fullerene were also presented in [132]. In general, the advantage of the apertureless SNOM technique over a conventional SNOM was not clearly shown in these first papers.

An approach–retraction test to prove the near-field nature of the collected signal was also done in [133] for a thin layer of sulfur. A TERS spectrum of fullerene C_{60} was initially located on a mica substrate and adhered to the tip during the surface scanning. Raman scattering enhanced by the tip increases the scattering cross section of a molecule under study by 7–8 orders of magnitude [24], and according to the estimates contained in the paper being cited, it corresponds to nearly 100 molecules. It is shown with a TERS system based on a tunnel current feedback sensor that a TERS signal collected on a Malachite Green dye appears on contact and disappears on tip retraction. It is also shown that such a dramatic enhancement of the interaction cross section causes a noticeable broadening of Raman lines.

Dye bleaching under focused high-intensity light is mentioned in [24]. Similar observations (CN^- ions on gold, Malachite Green isothiocyanate on gold, platinum probing tip) were reported in [134]. As a rule, the Raman signal is rather weak (e.g., with aperture-defined SNOM [135], an accumulation of the Raman signal on a raster of 32×32 point dimensions required 10 h; other papers report 9 h [136]). Apertureless SNOM may provide a significant gain in signal collection. In [137], apertureless modification of SNOM (with the tunnel current principle of topography feedback) required an acquisition time of 3 s per spectrum and made it possible to obtain the spectrum of a single molecule (Fig. 12).

The TERS method is widely used to investigate biological objects. The cells of *Staphylococcus Epidermidis* ATCC359 were studied in [138], and TERS spectra were obtained at several points of a SNOM map. Changes in Raman spectra suggest that the proteins migrate within a membrane at 20–200 nm. A table of spectral lines of different biological molecules is also given in [138]. The TERS map of K15 (cytokeratin 15)-positive human hair follicle ePCs (epithelial

progenitor cells) [139] was compared in [128] to a micro-Raman map. It was shown that the TERS resolution is several dozen times better. The Raman spectra of a *cytochrome c* protein containing Fe in different oxidation numbers, Fe-II, and Fe-III, were acquired in [140] during TERS scanning of an isolated mitochondrion (the spectra were acquired along a line on a sample surface with a step of 8 nm). The spectra clearly indicate a change in the Fe oxidation state in the protein caused by the scanning of the probe. Successful attempts at DNA scanning have been reported. The fundamental possibility of distinguishing amino acids by their TERS response was demonstrated on thymine and cytosine [141] in 2006. The spectra of adenine, thymine guanine, and cytosine in picomolar amounts were obtained by TERS also in [142]. RNA sequencing with TERS microscopy was also reported in [143], although insufficient probe resolution was noted.

Because biological molecules are designed to operate in water, it is extremely important for biologists to ensure the operation of the TERS microscope in a liquid. Successful attempts are reported in [144] to solve this problem technically.

It is useful to note that some gradient effects should be expected in SNOM systems [145], caused by an inhomogeneity of the electromagnetic field around the tip apex. Hence, the spectra obtained with TERS can differ from those obtained in ‘classical’ spectroscopy when the investigated molecule is located in the field of a plane wave. In TERS measurements, the selection rules caused by the symmetry of molecular wave functions can significantly differ from the ‘classical’ ones.

Raman scattering provides some freedom in the geometry of the experiment compared to the elastic tip scattering mode. The polarization of the pump and the Stokes component need not coincide. Nevertheless, the dipole oscillations in a probe tip most effectively interact with external light waves when their E vector is directed along the tip shaft, and this should be kept in mind. Scanning systems designed specially for an ASNOM operation [99]

enable the application and collection of light in the optimal direction (as a rule, from several sides). If some other AFM head is modified to be used in an ASNOM mode, the options offered by the instrument may be somewhat reduced. The pump radiation was directed in [146, 147] to the sample through the underside of a transparent substrate (from the bottom, in the traditional geometry for conventional microscopy), and it was proposed to use radially polarized light and a high-NA lens with a large proportion of sliding rays, in order to increase the efficiency of the interaction of light wave modes with the tip.

Because the interaction of electron density oscillations in the object under study with dipole oscillations in the probing tip for TERS systems does not fundamentally differ from other modifications of ASNOMs, the lateral resolution is also determined by the radius of the tip. In various studies, it is reported to be 10 nm [138], 10–20 nm [141], 20 nm [148], 40 nm [147], 50 nm [131], 55 nm [132], and 100 nm [24, 134]. In any case, it is possible to claim that a lateral resolution of TERS is much better than the resolution of the conventional Raman microscopy, which is determined by the Abbe limit of some part of the wavelength.

5.2 Photoluminescence

The efficiency of ASNOMs in collecting the luminescence spectra of CdSe quantum dots in ZnS was demonstrated in [149]. The work shows approach curves indicating an apparent (up to 10-fold) increase in the photoluminescence signal collected at a tip-to-surface distance of less than 5 nm. The optical lateral resolution was reported to be 10 nm. Similar CdSe/ZnS quantum dots with a characteristic size of 4 nm were used in [150]. It was shown that for the density of quantum dots used, $14 \mu\text{m}^{-2}$, an ASNOM can distinguish single quantum dots in the image. An optical approach curve (the dependence of the collected signal on the tip-sample separation) is reported in [151] for a CdSe/ZnS quantum dot, acquired with an Si probe, Au-coated probe, and a probe fabricated from a fullerene tube. The characteristic distance at which the photoluminescence significantly grows is about 7–10 nm. It is mentioned in the paper that the presence of a metallized tip in the vicinity of a quantum dot significantly increases the quantum yield of some states (found to be relatively weak in a free-standing quantum dot) and reduces the quantum yield of other states (which dominate in a free-standing quantum dot). Changes in the quantum yield of different states in a quantum dot caused by the presence of a fullerene nanotube nearby are also mentioned in [152].

The registration of the fluorescence spectrum of a single molecule using a gold ball 80 nm in diameter fixed at the tip of a conventional (tapered fiber) probe demonstrates sufficient sensitivity and resolution of ASNOMs [153]. In that paper, the signal dependence on the tip-object distance was also investigated (a sharp increase in the signal occurs at a distance of 15 nm on the approach curve), as was the shape of the optical images taken from a known point-like source. The shape of a collected image undoubtedly demonstrates a ‘dipole’ symmetry, indicating that some polarization on the surface plane is clearly preferable. To improve the matching of the incident wave and oscillations in the dipole of the probe, radial-polarized light was used in the lens. For a scanning system designed to operate in water, it was shown [154] that its sensitivity is also sufficient for single-molecule spectroscopy. An ASNOM system for scanning and lumines-

cence spectroscopy (with a tip fixed on a tuning fork) is also presented in [155]. We note that the unsuccessfully chosen geometry of the device (with the irradiating and collected light beams directed along the tip shaft) limits the quality of the two-photon spectra being collected; however, raster scattering scanning (using a much stronger signal) provides very clean images.

6. Conclusions. Summary

Scanning near-field optical microscopy (especially apertureless scanning near-field optical microscopy) as an optical technique to provide addressable optical access to a region whose size is arbitrarily smaller than the wavelength of light was apparently beyond reach prior to 1986. In reality, it is only a matter of changing the idea of how an electromagnetic field is applied to an object. From the wave principle (which, like all wave optics/radiophysics, does not allow the wave to be focused into a region much smaller than the wavelength), researchers switched to transmitting a signal along a wire that could be brought to the object with an accuracy determined by the size of the probe tip. At the industrial current frequency of 50 Hz and the wavelength of 6000 km, equal to the radius of the globe, it is not surprising that a voltmeter can locate an outlet wire with millimeter accuracy.

An ASNOM probe (metallized AFM tip) is an extremely efficient tool to match an external electromagnetic field with the local fields around a nano-object. The amplitude of the local field around the tip apex is 4–5 orders of magnitude higher than that in the plane wave used for excitation. Vice versa, the efficiency of light emission (luminescence or Raman) by a single molecule into the ambient space is enhanced for the same reasons.

Due to the similarity of its operational principle (a dipole rod antenna connected to the surface being investigated via a capacitor gap), ASNOMs allow the use of simple analytic models. These models in most cases allow describing the phenomena quantitatively, or, in the case of more detailed numerical simulations, checking their results based on ‘common sense’ grounds.

A signal collected by an sSNOM (ASNOM of ‘elastic’ light scattering) is a product of two quantities: the local field at the tip location point and the effective polarizability of the tip in the presence of a surface, which depends on the local value of the sample dielectric function. In many cases, one of these two factors could be assumed to be constant (and therefore an ASNOM image could be interpreted as a map of the other factor). But we must not forget that a simultaneous change in both factors in product (3) can dramatically complicate the interpretation of results.

It should also be kept in mind that the inhomogeneity of the field near the tip can change the selection rules for quantum transitions in a molecule being studied, which are known in classical spectroscopy from experience in applying a homogeneous field of a plane wave to an object.

6.1 What should an ‘ideal’ ASNOM look like?

From the standpoint of instrumentation, a modern ASNOM system should most probably meet the following requirements:

- it should include a scanning head similar to the AFM head that allows optical access to the probe tip, preferably at an angle of 20° – 30° to the sample surface. The principle of operation of the feedback sensor—AFM Tap-

pingModeTM — has been proved to be quite good. Meanwhile, the JumpingModeTM of nonresonance periodic approach–retraction cycles opens additional possibilities for ASNOMs, although such a mode may reduce the scanning rate;

— the objective ‘lens’ that focuses the exciting beam onto the probe and collects light scattered by the tip should consist purely of mirrors (in order to maintain the capability of the ASNOM itself to operate in the near IR, middle IR, far IR, and visible ranges) [156]. The mechanical design should allow coarse and precise positioning of the focus relative to the tip to compensate the tip position tolerance caused by a probe reload;

— the optical setup should include an interferometer (preferably Michelson) to enhance the signal by optical homo-(hetero-)odyning. The reference arm of the interferometer should allow its length modulation of at least half the working wavelength, with a modulation period of a few milliseconds. The electronics detecting the near-field signal component in the photocurrent should use at least two positions of the reference beam mirror (two phases of the homodyne signal) in order to fully exploit the ability of the ASNOM to measure the amplitude and phase of the signal simultaneously. There may be an optional presence in the interferometer of an element that allows modulating the length of the reference arm by several centimeters, in order to provide a change in the delay of the probing light pulse with respect to the signal pulse in the case of operation with ultrashort light pulses or, in the case of using a Michelson interferometer as a Fourier-transform spectrometer, to measure the spectrum of the tip inelastic optical response (luminescence and Raman);

— the system should include a laser that operates at the wavelengths of interest, preferably with a wavelength tuning option. The laser radiation should be stable in power, should be monochromatic, and have a good transverse structure TEM₀₀, because all of that determines the low-noise operation of optical homodyning.

In many experiments, the following options may also be useful: the ability to apply electrical signal(s) to the sample, heating or cooling the sample, and the ability to fill the optical path with a nonabsorbing gas.

All these requirements are feasible, and these elements have already been used, together or separately, in successful designs of home-made ASNOMs. A complete ASNOM system is commercially offered by Neaspec GmbH (Germany). Their instruments have just a single substantial disadvantage, their price.

Acknowledgments

One of the authors takes the opportunity to thank F Keilmann as a teacher and R Hillenbrand for his kind help in studies of the ASNOM technique.

References

- Pohl D W, Denk W, Lanz M *Appl. Phys. Lett.* **44** 651 (1984)
- Binnig G, Rohrer H “Scanning tunneling microscope”, US Patent 4,343,993 (1982); <http://www.google.com/patents/US4343993>
- Dürig U, Pohl D W, Rohner F J *Appl. Phys.* **59** 3318 (1986)
- Betzig E et al. *Biophys. J.* **49** 269 (1986)
- Betzig E et al. *Science* **251** 1468 (1991)
- Obermüller C, Karrai K *Appl. Phys. Lett.* **67** 3408 (1995)
- Bethe H A *Phys. Rev.* **66** 163 (1944)
- Novotny L, Hafner C *Phys. Rev. E* **50** 4094 (1994)
- Valaskovic G A, Holton M, Morrison G H *Appl. Opt.* **34** 1215 (1995)
- Cherkun A P et al. *Rev. Sci. Instrum.* **77** 033703 (2006)
- Wickramasinghe H, Williams C, “Apertureless near field optical microscope”, US Patent 4,947,034 (1990); <http://www.google.com/patents/US4947034>
- Zenhausen F, Martin Y, Wickramasinghe H K *Science* **269** 1083 (1995)
- Inouye Y, Kawata S *Opt. Lett.* **19** 159 (1994)
- Hamann H F, Gallagher A, Nesbitt D J *Appl. Phys. Lett.* **73** 1469 (1998)
- Martin Y, Zenhausen F, Wickramasinghe H K *Appl. Phys. Lett.* **68** 2475 (1996)
- Bek A, Vogelgesang R, Kern K *Rev. Sci. Instrum.* **77** 043703 (2006)
- Bridger P M, McGill T C *Opt. Lett.* **24** 1005 (1999)
- Denk W, Pohl D W J. *Vac. Sci. Technol. B* **9** 510 (1991)
- Novotny L, Hecht B *Principles of Nano-Optics* (Cambridge: Cambridge Univ. Press, 2006)
- Novotny L, Stranick S J *Annu. Rev. Phys. Chem.* **57** 303 (2006)
- Binnig G, Quate C F, Gerber Ch *Phys. Rev. Lett.* **56** 930 (1986)
- Ordal M A et al. *Appl. Opt.* **24** 4493 (1985)
- Martin O J F, Girard C *Appl. Phys. Lett.* **70** 705 (1997)
- Neacsu C C et al. *Phys. Rev. B* **73** 193406 (2006)
- Cvitkovic A, Ocelic N, Hillenbrand R *Opt. Exp.* **15** 8550 (2007)
- Renger J et al. *J. Opt. Soc. Am. A* **21** 1362 (2004)
- Zhang L M et al. *Phys. Rev. B* **85** 075419 (2012)
- Cvitkovic A et al. *Phys. Rev. Lett.* **97** 060801 (2006)
- Brehm M et al. *Opt. Exp.* **16** 11203 (2008)
- Jin J *The Finite Element Method in Electromagnetics* 3rd ed. (Hoboken, NJ: John Wiley and Sons Inc., 2014)
- Leontovich M A, Levin M L *Zh. Tekh. Fiz.* **14** 481 (1944)
- Ramo S, Whinnery J R *Fields and Waves in Modern Radio* (New York: J. Wiley and Sons, 1944); Translated into Russian: *Polya i Volny v Sovremennoi Radiotekhnike* (Moscow–Leningrad: Gos-tekhnizdat, 1948)
- Jackson J D *Classical Electrodynamics* 3rd ed. (New York: Wiley, 1999)
- Novotny L, Bian R X, Xie X S *Phys. Rev. Lett.* **79** 645 (1997)
- Zayats A V *Opt. Commun.* **161** 156 (1999)
- Martin Y C, Hamann H F, Wickramasinghe H K *J. Appl. Phys.* **89** 5774 (2001)
- Madrazo A et al. *J. Opt. Soc. Am. A* **15** 109 (1998)
- Hillenbrand R, Keilmann F *Appl. Phys. B* **73** 239 (2001)
- Mie G *Ann. Physik* **330** 377 (1908)
- McLeod A S et al. *Phys. Rev. B* **90** 085136 (2014)
- Huber A et al. *Adv. Mater.* **19** 2209 (2007)
- Keilmann F, Hillenbrand R *Philos. Trans. Math. Phys. Eng. Sci.* **362** 787 (2004)
- Osad'ko I S *Phys. Usp.* **53** 77 (2010); *Usp. Fiz. Nauk* **180** 83 (2010)
- Knoll B, Keilmann F *Nature* **399** 134 (1999)
- Taubner T, Keilmann F, Hillenbrand R *Opt. Exp.* **13** 8893 (2005)
- Hillenbrand R, Keilmann F *Phys. Rev. Lett.* **85** 3029 (2000)
- Huber A et al. *Nano Lett.* **6** 774 (2006)
- Batchelder J S, Taubenblatt M A *Appl. Phys. Lett.* **55** 215 (1989)
- Vaez-Iravani M, Toledo-Crow R *Appl. Phys. Lett.* **62** 1044 (1993)
- Ignatovich F V, Novotny L *Phys. Rev. Lett.* **96** 013901 (2006)
- Taubner T, Hillenbrand R, Keilmann F J. *Microsc.* **210** 311 (2003)
- Gomez L et al. *J. Opt. Soc. Am. B* **23** 823 (2006)
- Stebounova L, Akhremitchev B B, Walker G C *Rev. Sci. Instrum.* **74** 3670 (2003)
- Kazantsev D V, Kazantseva E A *Prib. Tekh. Eksp.* (5) 120 (2014)
- Taubner T, Keilmann F, Hillenbrand R *Nano Lett.* **4** 1669 (2004)
- Kazantsev D, Ryssel H *Appl. Phys. A* **113** 27 (2013)
- Zhong Q et al. *Surf. Sci. Lett.* **290** L688 (1993)
- Labardi M, Patanè, Allegrini M *Appl. Phys. Lett.* **77** 621 (2000)
- Maghelli N et al. *J. Microsc.* **202** 84 (2001)
- Hillenbrand R, Knoll B, Keilmann F J. *Microsc.* **202** 77 (2001)
- Wang L, Xu X G *Nature Commun.* **6** 9973 (2015)
- Esteban R et al. *Nano Lett.* **8** 3155 (2008)
- Ocelic N, Huber A, Hillenbrand R *Appl. Phys. Lett.* **89** 101124 (2006)
- Xu X G et al. *J. Phys. Chem. Lett.* **3** 1836 (2012)
- Pollard B et al. *Nature Commun.* **5** 3587 (2014)

66. Kazantsev D “Artifact-free data recovery system for an ASNOM application”, arXiv:1307.2563
67. Bechtel H A et al. *Proc. Natl. Acad. Sci. USA* **111** 7191 (2014)
68. Xu X G, Raschke M B *Nano Lett.* **13** 1588 (2013)
69. Xu X G, Gilburd L, Walker G C *Appl. Phys. Lett.* **105** 263104 (2014)
70. Huth F et al. *Nano Lett.* **12** 3973 (2012)
71. Stiegler J M et al. *ACS Nano* **5** 6494 (2011)
72. Berweger S et al. *J. Am. Chem. Soc.* **135** 18292 (2013)
73. Amenabar I et al. *Nature Commun.* **4** 2890 (2013)
74. Huth F et al. *Nature Mater.* **10** 352 (2011)
75. Albrecht T R et al. *J. Appl. Phys.* **69** 668 (1991)
76. Dürig U, Steinauer H R, Blanc N J. *Appl. Phys.* **82** 3641 (1997)
77. Giessibl F J *Rev. Mod. Phys.* **75** 949 (2003)
78. Elings V, Gurley J “Jumping probe microscope”, US Patent 5,266,801 (1993)
79. Drude P *Ann. Physik* **306** 566 (1900)
80. Wada N et al. *J. Non-Cryst. Solids* **43** 7 (1981)
81. Brendel R, Bormann D J. *Appl. Phys.* **71** 1 (1992)
82. Kim Z H et al. *Nano Lett.* **7** 2258 (2007)
83. Xu X G et al. *J. Phys. Chem. C* **120** 1945 (2016)
84. von Ribbeck H-G et al. *Opt. Exp.* **16** 3430 (2008)
85. Huber A J et al. *Nano Lett.* **8** 3766 (2008)
86. Zhan H et al. *Appl. Phys. Lett.* **91** 162110 (2007)
87. Stiegler J M et al. *Nano Lett.* **10** 1387 (2010)
88. Hubert C, Levy J *Appl. Phys. Lett.* **73** 3229 (1998)
89. Lucas I T et al. *Nano Lett.* **15** 1 (2015)
90. Stebounova L V et al. *J. Appl. Phys.* **101** 124306 (2007)
91. Taniguchi K, Kanemitsu Y *Jpn. J. Appl. Phys.* **44** 575 (2005)
92. Yang H U et al. *Rev. Sci. Instrum.* **84** 023701 (2013)
93. Brehm M et al. *Nano Lett.* **6** 1307 (2006)
94. Taubner T, Hillenbrand R, Keilmann F *Appl. Phys. Lett.* **85** 5064 (2004)
95. Fei Z et al. *Nano Lett.* **11** 4701 (2011)
96. Fei Z et al. *Nano Lett.* **15** 4973 (2015)
97. Taubner T et al. *Science* **313** 1595 (2006)
98. Kazantsev D V *JETP Lett.* **83** 323 (2006); *Pis'ma Zh. Eksp. Fiz.* **83** 380 (2006)
99. Kazantsev D V, Ryssel H *Mod. Instrum.* **2** (2) 33 (2013)
100. Huber A, Ocelic N, Kazantsev D, Hillenbrand R *Appl. Phys. Lett.* **87** 081103 (2005)
101. Barron T H K *Phys. Rev.* **123** 1995 (1961)
102. Ruppini R, Englman R *Rep. Prog. Phys.* **33** 149 (1970)
103. Mills D L, Burstein E *Rep. Prog. Phys.* **37** 817 (1974)
104. Bimberg D et al. *Physics of Group IV Elements and III-V Compounds. Physik der Elemente der IV. Gruppe und der III-V Verbindungen* (Landolt-Börnstein, Numerical Data and Functional Relationships, Vol. 17, Pt. 1) (Berlin: Springer, 1981)
105. Sasaki Y et al. *Phys. Rev. B* **40** 1762 (1989)
106. Zayats A V, Smolyaninov I I, Maradudin A A *Phys. Rep.* **408** 131 (2005)
107. Rockstuhl C, Salt M G, Herzig H P *J. Opt. Soc. Am. B* **22** 481 (2005)
108. Huber A, Ocelic N, Hillenbrand R *J. Microscopy* **229** 389 (2008)
109. Huber A J et al. *Appl. Phys. Lett.* **92** 203104 (2008)
110. Krenn J R et al. *J. Microscopy* **209** 167 (2003)
111. Xu X G et al. *Nature Commun.* **5** 4782 (2014)
112. Gilburd L et al. *J. Phys. Chem. Lett.* **7** 289 (2016)
113. Schnell M et al. *Nature Photon.* **3** 287 (2009)
114. Dorfmueller J et al. *Nano Lett.* **11** 2819 (2011)
115. Schnell M et al. *J. Phys. Chem. C* **114** 7341 (2010)
116. Hillenbrand R et al. *Appl. Phys. Lett.* **83** 368 (2003)
117. Chen J et al. *Nature Lett.* **487** 77 (2012)
118. Fei Z et al. *Nature Nanotechnol.* **8** 821 (2013)
119. Gerber J A et al. *Phys. Rev. Lett.* **113** 055502 (2014); arXiv:1404.4668
120. Ni G X et al. *Nature Mater.* **14** 1217 (2015)
121. Wagner M et al. *Nano Lett.* **14** 894 (2014)
122. Wagner M et al. *Nano Lett.* **14** 4529 (2014)
123. Pettinger B, in *Surface-Enhanced Raman Scattering: Physics and Applications* (Topics in Applied Physics, Vol. 103, Eds K. Kneipp, M. Moskovits, H. Kneipp) (Berlin: Springer, 2006) p. 217
124. Young M A, Dieringer J A, Van Duyne R P, in *Tip Enhancement* (Eds S. Kawata, V. M. Shalaev) (Amsterdam: Elsevier, 2007) p. 1
125. Bailo E, Deckert V *Chem. Soc. Rev.* **37** 921 (2008)
126. Deckert V J. *Raman Spectrosc.* **40** 1336 (2009)
127. Domke K F, Pettinger B *ChemPhysChem* **11** 1365 (2010)
128. Treffer R et al. *Biochem. Soc. Trans.* **40** 609 (2012)
129. Kumar N et al. *EPJ Tech. Instrum.* **2** 1 (2015)
130. Tarun A et al. *Rev. Sci. Instrum.* **79** 013706 (2008)
131. Hayazawa N et al. *Opt. Commun.* **183** 333 (2000)
132. Stöckle R M et al. *Chem. Phys. Lett.* **318** 131 (2000)
133. Anderson M S *Appl. Phys. Lett.* **76** 3130 (2000)
134. Pettinger B et al. *Phys. Rev. Lett.* **92** 096101 (2004)
135. Jahncke C L, Paesler M A, Hallen H D *Appl. Phys. Lett.* **67** 2483 (1995)
136. Webster S, Smith D, Batchelder D *Vib. Spectrosc.* **18** 51 (1998)
137. Zhang R et al. *Nature* **498** 82 (2013)
138. Neugebauer U et al. *ChemPhysChem* **7** 1428 (2006)
139. Tiede S et al. *Stem Cells* **27** 2793 (2009)
140. Bohme R et al. *Chem. Commun.* **47** 11453 (2011)
141. Rasmussen A, Deckert V J. *Raman Spectrosc.* **37** 311 (2006)
142. Domke K F, Zhang D, Pettinger B J. *Am. Chem. Soc.* **129** 6708 (2007)
143. Bailo E, Deckert V *Angew. Chem. Int. Ed.* **47** 1658 (2008)
144. Schmid T et al. *J. Raman Spectrosc.* **40** 1392 (2009)
145. Ayars E J, Hallen H D, Jahncke C L *Phys. Rev. Lett.* **85** 4180 (2000)
146. Dorn R, Quabis S, Leuchs G *Phys. Rev. Lett.* **91** 233901 (2003)
147. Hayazawa N, Saito Y, Kawata S *Appl. Phys. Lett.* **85** 6239 (2004)
148. Domke K F, Zhang D, Pettinger B J. *Am. Chem. Soc.* **128** 14721 (2006)
149. Gerton J M et al. *Phys. Rev. Lett.* **93** 180801 (2004)
150. Xie C et al. *Appl. Phys. Lett.* **89** 143117 (2006)
151. Shafran E, Mangum B D, Gerton J M *Phys. Rev. Lett.* **107** 037403 (2011)
152. Shafran E, Mangum B D, Gerton J M *Nano Lett.* **10** 4049 (2010)
153. Anger P, Bharadwaj P, Novotny L *Phys. Rev. Lett.* **96** 113002 (2006)
154. Frey H G, Paskarbit J, Anselmetti D *Appl. Phys. Lett.* **94** 241116 (2009)
155. Nowak D B, Lawrence A J, Sánchez E J *Appl. Opt.* **49** 6766 (2010)
156. Hillenbrand R, Keilmann F “Spiegeloptik für nahfeldoptische Messungen”, DE Patent App. DE200,610,002,461 (2007); <https://www.google.com/patents/DE102006002461A1?cl=ru>